ANALYSIS AND EVALUATION OF FRAGMENT SIZE DISTRIBUTIONS IN ROCK BLASTING AT THE ERDENET MINE

By

Erdenebaatar Dondov

RECOMMENDED:

Dr. Tathagata Ghosh
Advisory Committee Member

Dr. Rajive Ganguli
Advisory Committee Member

Dr. Gang Chen
Advisory Committee Chair

APPROVED:

Dr. Rajive Ganguli, Chair
Department of Mining and Geological Engineering

4/24/15

Date

ANALYSIS AND EVALUATION OF FRAGMENT SIZE DISTRIBUTIONS IN ROCK BLASTING AT THE ERDENET MINE

A

PROJECT

Presented to the Faculty of the University of Alaska Fairbanks

In Partial Fulfillment of the Requirements

For the Degree of

MASTER OF SCIENCE

By

Erdenebaatar Dondov

Fairbanks, AK

April 2015

Abstract

Rock blasting is one of the most important operations in mining. It significantly affects the subsequent comminution processes and, therefore, is critical to successful mining productions.

In this study, for the evaluation of the blasting performance at the Erdenet Mine, we analyzed rock fragment size distributions with the digital image processing method. The uniformities of rock fragments and the mean fragment sizes were determined and applied in the Kuz-Ram model. Statistical prediction models were also developed based on the field measured parameters. The results were compared with the Kuz-Ram model predictions and the digital image processing measurements.

A total of twenty-eight images from eleven blasting patterns were processed, and rock size distributions were determined by Split-Desktop program in this study. Based on the rock mass and explosive properties and the blasting parameters, the rock fragment size distributions were also determined with the Kuz-Ram model and compared with the measurements by digital image processing. Furthermore, in order to improve the prediction of rock fragment size distributions at the mine, regression analyses were conducted and statistical models were developed for the estimation of the uniformity and characteristic size.

The results indicated that there were discrepancies between the digital image measurements and those estimated by the Kuz-Ram model. The uniformity indices of image processing measurements varied from 0.76 to 1.90, while those estimate by the Kuz-Ram model were from 1.07 to 1.13. The mean fragment size of the Kuz-Ram model prediction was 97.59% greater than the mean fragment size of the image processing. The multivariate nonlinear regression analyses conducted in this study indicated that rock uniaxial compressive strength and elastic modulus, explosive energy input in the blasting, bench height to burden ratio and blast area per hole were significant predictor variables in determining the fragment characteristic size and the uniformity index. The regression models developed based on the above predictor variables showed much closer agreement with the measurements.

Table and Contents

List of Figures

Page

List of Tables

Page

List of Appendices

Page

ACKNOWLEDGEMENTS

I would like to express my deepest and sincere gratitude to my advisor, Dr. Gang Chen, and my thesis committee members, Dr. Rajive Ganguli and Dr. Tathagata Ghosh, for their support and guidance throughout this project. Their continued support led me to the right way.

I would also like to extend my appreciation to Dr. Nyamdorj Dendev for his advice and my colleague, Temuujin Ulambayar, for his assistance during my study.

My deepest gratitude goes to the Department of Mining and Geological Engineering at University of Alaska Fairbanks for providing scholarship and the Erdenet Mining Corporation for funding for this study.

I would also like to extend my sincere appreciation to my wife and my daughters for their love, trust, and support. Without their encouragement, I would not have a chance to complete this project.

Chapter 1 Introduction

Optimum fragment size distribution is known as one of the important quality factors of rock blasting. Continued improvement of rock blasting operations is essential in mining production in order to achieve economic efficiency and maintain mining safety.

Over the years, scientists and engineers have contributed efforts to the development of new models and methods for field measuring and analyses of fragment size distributions. A number of techniques have been successful for practical applications of fragment size measurements and analyses. Effective measurements and estimations of blasting fragment size have proved to play an influential role in mining productivity.

This study will focus on the measurements and analyses of blasting fragment size distributions at the Erdenet Mine in Mongolia. A number of researchers have conducted studies on blasting efficiency at the Erdenet Mine, for example, Nyamdorj.D, (2006), who measured and determined the mean fragment size to be 235 mm at some blasting rounds using the planimetric method. In the current study, the updated and improved measurements and analyses of blasting fragment size distributions at the mine were conducted with the applications of the digital image processing method.

1.1 Objectives of the Study

This study contains the following three objectives:

- Measurements and analyses of blasting fragment size by the digital image processing method
- Comparison of blasting fragment size distributions between the measurements and predictions by the Kuz-Ram model
- Development of statistical prediction models for the blasting fragment size distributions based on site-specific blasting parameters at the Erdenet Mine.

1.2 Proposed Approaches

Three main methods were used in this study: the digital image processing method for fragment size measurements, the Kuz-Ram model for size distribution prediction and the multivariate nonlinear regression analysis for improved mine site specific prediction model development.

In this study, muckpile images of eleven blasted patterns were collected at the Erdenet Mine from September 2013 to August 2014 and the Split-Desktop was employed for size measurements. Split-Desktop is a popular image processing system and has been widely used in the rock blasting industry.

The measurements were compared with the well-known Kuz-Ram model, a blast fragment size distribution prediction method developed by Cunningham (1983). The measured and predicted results were plotted and compared for each blasting pattern and rock properties. The uniformity of size distribution was determined based on curve shape.

Furthermore, the key parameters in defining rock fragment size distribution curves, which include the uniformity index and the characteristic size were analyzed based on a number of critical predictor variables such as rock properties, explosive energy input and blasting geometry employing the nonlinear multivariate regression analysis method. Statistical prediction models were developed for the estimation of the uniformity index and the characteristic size for the Erdenet Mine.

Chapter 2 Literature Review

2.1 Blasting Theory and Main Factors

As described by Atlas Powder Co. (1987), in rock blasting, the rock mass is affected by a detonating explosive in three principal stages. In the first stage, starting from the initiation point, the blasthole expands under the extremely high detonating pressure by crushing the blasthole walls. In the second stage, compressive stress waves emanate in all directions from the blasthole with a velocity equal to the sonic wave velocity in the rock. When these compressive stresses reach the interface between the rock mass and the free face, it reflects back as tensile stresses. If the tensile strength of the rock is exceeded, the rock breaks in the burden area.

In the third stage, the released gas volume "enters" the crack formation under high pressure, expanding the cracks. If the distance between the blasthole and the free face is correctly calculated, the rock mass between the blasthole and the free face will yield and be thrown forward.

The explosives reaction in the blasthole is very fast and the effective work of the explosive is considered completed when the blasthole volume has expanded to 10 times its original volume, which takes approximately 5 ms (Stig Olofsson,1990).

2.1.1 Rock Blasting Mechanism (Atlas Powder Co, 1990)

According to Atlas Powder Co (1990), a rock blasting can generally be broken down into four time frames: detonation, shock or stress wave propagation, gas pressure expansion, and mass movement.

Detonation: The initial phase of the rock fragmentation process is detonation. When an explosive is detonated, the sudden release of energy and reaction products at high pressure (~40000atm) and high temperature (3000°-7000°K) by rapid chemical reaction.

$$P_{DET(atm)} = 2.5\ \rho_e (VOD)^2 \qquad (2.1)$$

$P_{DET(atm)}$- detonation pressure (atm)

ρ_e – explosive density (kg/m^3)

VOD – velocity of detonation (km/s)

Explosion pressure to the wall of the blasthole,

$$Pe = \frac{P_{DET}}{2} \qquad (2.2)$$

Where, P_e - borehole pressure (atm).

The velocity of detonation is greater than the velocity of sound in the explosive.

Table 2.1 Detonation pressures for selected explosives (Atlas Powder Co, 1987)

Explosive	Density (g/cc) / (kg/m3)	VOD (ft/sec) / (m/sec)	Detonation pressure (kbar) / (atm)	Pressure (psi)
ANFO	0.81/ 810	12,000/ 3,660	27/ 26,645	391,600
Emulsion, High Explosive	1.19/ 1190	19,000/ 5,790	100/ 98,690	1,450,400
Ammonia Gelatin Dynamite	1.40/ 1400	20,000/ 6,100	130/ 128,300	1,885,500
Composition B	1.60/ 1600	26,000/ 7,925	251/ 247,715	3,640,500

High velocity of detonation explosives are used as initiation for lower velocity of detonation explosives (ANFO).

Shock Wave Propagation: The second phase, immediately following detonation, is the shock and stress wave propagation throughout the rock mass.

Generally, extensive compressive, shear, and tensile failure occurs as a region of pulverized material since the wave energy is at its maximum near the borehole wall.

The tangential stress, if large enough, can cause tensile failures at right angles to the direction of propagation. These pressure waves transmit through the rock mass, and from the rapidly expanding high-pressure gas, impact the borehole wall.

In a typical, bottom primed, cylindrical shot hole in bench blasting, the strain waves originally formed near the point of initiation are already in progress, and stress, if large enough, can cause tensile failures at right angles to the direction of propagation. The strain wave propagation is more like that shown in Figure 2.1.

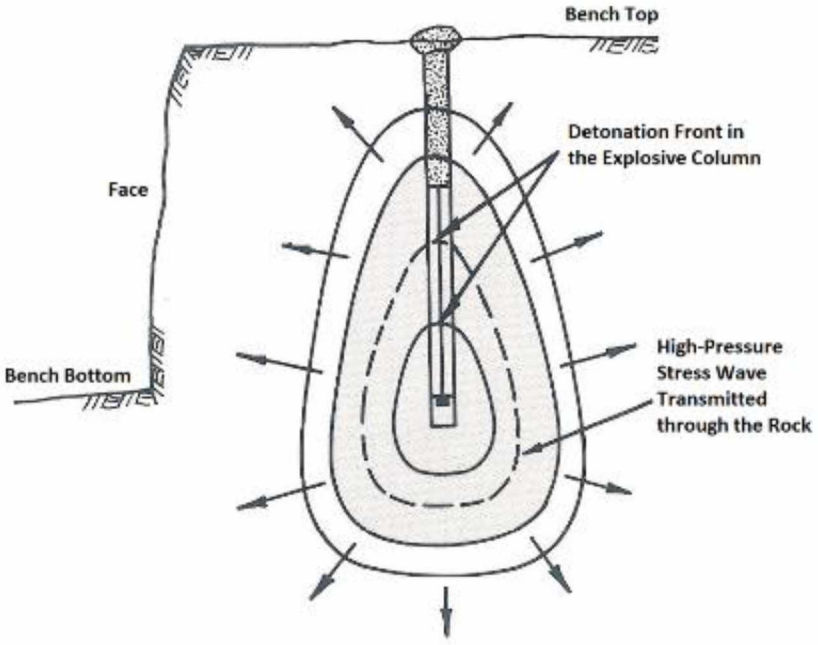

Figure 2.1 Section through the face during detonation showing expanding stress wave front (Atlas Powder Co, 1987)

As a shock wave is transmitted into the medium surrounding the charge in a blasthole, the shock wave amplitude and energy decrease with distance from the hole. As the shock propagates radially from the blasthole, the amplitude decreases rapidly and soon reaches limit for plastic deformation in one-dimensional compression. Such elastic compression waves are called stress waves, and they propagate with the velocity of sound (340m/s). When the stress wave travels into a new medium with a different impedance, a fraction of the energy will be reflected and another fraction will be transmitted.

Gas Pressure Expansion: During and after the stress wave propagation, the high-pressure, high-temperature gases generate a stress field around the blasthole that can expand the original hole, and extend radial cracks, and jet into any discontinuities.

At this stage, the fracture network in the rock mass is either fully developed or under development. Gas confinement time may vary from 5 to 110ms; this variation depends on amount and type of explosive, rock material type, geological structure, stemming, and burden and spacing.

The confinement in generally decreases by using higher energy explosive or with less burden.

Mass Movement: At this stage, the additional fragmentation is performed by in-flight collisions and impacts with the ground. And rock mass movement is carried out based on rock mass properties.

a) Hard rock with largely spaced joints- entire length moves out with roughly equal velocity at every point.
b) Soft rock with closely jointed – burden moves out as flexural rupture.
c) Soft rock with subdrilling – burden moves out as flexural rupture; also, toe burden moves up at a greater angle to the horizontal (Atlas Powder Co, 1987).

2.1.2 Main Factors

Rock Mass Features (ISEE, 2011)

Rock structure is one of the most important geologic factors that affects blasting performance. There are three basic structures: bedding planes, faults, and joints. Bedding planes occur only in sedimentary rocks, but faults and joints can occur in all rock formation.

Bedding planes are surfaces that separate sedimentary rock layers that differ considerably from other beds. The bedding can be a positive rock blasting property, when it is strong enough to ensure confinement, its thickness approaches the desired fragmentation size, or it is located at a planned floor, roof, and wall location. In large projects, the blaster often has some latitude to change face orientation in order to take advantage of strike and dip, whereas, in smaller projects like in trenching, this opportunity does not exist.

Faults are fractures in rock where there has been relative displacement of the two sides. There are three basic types of faults: normal, reverse, and lateral faults.

Joints can be the result of tectonic forces sufficiently strong to fracture rock in place, or the contraction of cooling magma. Jointing occurrence alone divides the rock mass into preexisting blocks. Joint spacing is typically a good predictor of blast fragmentation size. Poor explosive energy distribution occurs when borehole patterns are larger than joint spacing. The joints can cause such as poor fragmentation, air over pressure, flyrock, and highwall failure.

Rock Mechanics Properties (ISEE, 2011)

Rock properties are usually specified for drillers and blasters by six common properties: density, hardness, porosity, strength, rock velocity, and elasticity.

Rock strength is measured as the force under which rock fails or breaks. Rock can fail in three ways: compression, tension, and shear. Rock is generally strongest in compression, so blast designs should strive to place the rock in tension for breakage and in shear for creating smooth surfaces, such as in presplitting.

Rock elasticity is the rock's ability to store the elastic energy of strain. The two constant measures most commonly used are: modulus of elasticity and Poisson's ratio.

The modulus of elasticity is often called Young's modulus, which is the ratio of applied stress to its corresponding strain in materials. Poisson's ratio is the ratio of the lateral unit strain to the longitudinal unit strain of a rock that has been stressed longitudinally within its elastic limit.

Rock porosity is a measure of the void space within a rock. These voids or open spaces can increase the potential for a rock to take in and possibly hold water. Extreme porosity can effectively reduce explosive energy confinement.

Rock velocity is the velocity at which rock transmits a shock wave. Typically, stronger and denser rocks have higher velocities than soft, weaker rocks.

Energy Input (Hustrulid, 1999)

In the case of the crusher, the electricity is that used to drive the electric motors. In blasting, the theoretical energy of the explosive is used.

For calculation of energy consumption of rock fragmentation by explosives, the most common three approaches are available. These are:

1) Rittinger 's Law, who suggested that the energy required was related to the amount of new surface area created. The work done (W) is the difference in the surface energies before and after crushing.

$$W = 6SF^3\left(\frac{1}{P}-\frac{1}{F}\right) = K_R\left(\frac{1}{P}-\frac{1}{F}\right) \qquad (1.3)$$

where W – total energy (work) required for size reduction from feed size (F) to product size (P)

F – feed diameter

P – product diameter

S – surface energy/unit area

K_R – the Rittinger's constant

2) Kick's Law states that the required energy is related to the total strain energy required by the particles to bring them to the point of failure (Hustrulid, 1999)

3) Bond's Law suggests that the particle must first be strained to the breaking point (volume dependence) and then new surface is created during failure (area dependence) that both processes must be involved.

$$W = K_B \left(\frac{1}{P^{\frac{1}{2}}} - \frac{1}{F^{\frac{1}{2}}} \right) \qquad (2.4)$$

Where W – work or energy input to a machine reducing material from a definite feed size to a definite product size (kWh/t)

F – diameter of the square hole that will pass 80% of the feed (microns)

P - diameter of the square hole that will pass 80% of the product (microns)

K_B – Bond's constant.

Bond's constant is determined by measuring amount of energy required to reduce a given feed to an given product. For example, an input energy of 3 kWh reduces 1 ton of material from a size 1600 microns to 400 microns.

If $K_B = W \frac{P^{\frac{1}{2}} \; F^{\frac{1}{2}}}{F^{\frac{1}{2}} - P^{\frac{1}{2}}} = 3 \frac{400^{\frac{1}{2}} \; 1600^{\frac{1}{2}}}{1600^{\frac{1}{2}} - 400^{\frac{1}{2}}} = 120 \; kWh - micron^{\frac{1}{2}}/t$

The calculation of the amount of energy required to reduce the material from infinite feed size to a product size of 100 microns.

$$W_i = K_B \left(\frac{1}{P^{\frac{1}{2}}} - \frac{1}{F^{\frac{1}{2}}} \right) = 120 \left(\frac{1}{100^{\frac{1}{2}}} - \frac{1}{\infty^{\frac{1}{2}}} \right) = 12 \; kWh/t$$

W_i is called the Bond work index. The index shows the comminution properties and the energy requirements for different materials and processes.

For applying the Bond work index in blasting is the converting of the explosive energy to electrical energy ((Hustrulid, 1999).

Energy consumption in blasting is of the order of 0.4-0.6 kWh/t, whereas in case of crushing and grinding it is 3-6 kWh/t and 10-30 kWh/t, respectively. This difference is due to the variations in product size, reduction ratio and discontinuous nature of boundary layers or cracks (Prasad,1994).

Protodyakonov Hardness Factor (Sandvik Tamrock, 1999)

This factor is primarily used in Russia for assessing both rock drillability and blastability. Protodyakonov established the following relationship between the relative rock hardness factor and the uniaxial compressive strength:

$$f = 0.1\,UCS \qquad (2.5)$$

Unfortunately, the Protodyakonov rock hardness factor does not differentiate between hardness of rocks beyond 200 MPa.

2.2 Size Distribution Measurements

The size distribution analysis of the rock fragmentation may be performed by two methods: sieving (direct) and image analysis (indirect). The first is a more accurate but more expensive measuring method; with this method, the samples of muckpile have to be sieved using different sizes of screens. Usually, researchers only use the sieving method for calibrating of image analysis systems. The second method is the most widely used method in the world, in which special image analysis software is employed used for the measuring of rock fragment size distributions. In this study, the image analysis method was used.

Measurement of the rock fragmentation helps us to evaluate the blasting quality or results. For this reason, image processing method has been developed for more than three decades. The photoanalysis was first proposed by Carlsan&Nyberg (1983). Since then, others continued to contribute to the development of photoanalysis techniques, such as Nie&Rustan (1987), Hunter et al. (1990), Farmer (1991), Stephansson et al. (1992), Kemeny (1993), Girdner (1996), Franklin et al. (1996) and others. Different companies or research centers had developed their own programs for measuring rock fragment size distributions. All of them used the similar method involving muck pile images. The developed programs include the IPACS system, the TUCIPS system, FRAGSCAN, Fragalyst, GoldSize, the WipFrag system and the SPLIT system. These techniques are variously based on greyscale and binary image analysis techniques including edge detection, thresholding, equalization, binary image morphology, region growing, and watershed segmentation.

All of these image analysis techniques use photographic greyscale images to capture the surface of a rock pile, and determine the size distribution from this sample. Measurement of fragment size of blasted rock is important in order to evaluate the efficiency of the production blasting

operation. There are several methods of size distribution measurement that fall under two broad categories: direct and indirect.

The sieve analysis is the direct and accurate method of measuring size distribution. Although it is the most accurate technique among others, it is not practical for such a large scale due to being both expensive and time-consuming. For this reason, indirect methods which are observational, empirical, and digital methods have been developed (Esen, 2000).

The observational method, which depends on an expert's common sense, is a widely used technique. An engineer assesses the fragmentation and other blasting results subjectively. This method is not a scientific method as it does not give any information about the size distribution.

Blasting parameters are considered to determine the size distribution in some empirical models such as Larsson's equation, SveDeFo formula, Kuz-Ram model, etc. (Esen, 2000).

Digital image processing programs allow rapid and accurate fragmentation size distribution evaluation of blasted rock. The most popular methods are SPLIT system, WipFrag system, Fragscan, and TUPICS.

TUCIPS system

TUCIPS (Technical University Clausthal Image Processing System) has been developed at Technical University Clausthal (Germany) to measure blast fragmentation. This system involves general algorithms of image processing and a specially created algorithm for muckpile image analysis. There is just a five-percent (5%) deviation in the practical test with this program, so this system is suitable for practical use (Havermann and Vogt, 1996).

WipFrag system

Using digital image analysis of rock photographs and videotape images with, granulometry system, grain size distribution may be obtained by WipFrag. Photographic images are digitized from slides, prints, or negatives by using WipFrag. In order to overcome size limitations inherent with a single image, WipFrag has the function for zoom-merge analysis. Therefore, combined analysis of images taken at different scales of observation may be analyzed. In addition, when using Edge Detection Variables (EDV), fragment boundaries are analyzed efficiently, and manual editing can improve edge detection (Maerz et al., 1996).

Fragalyst

The system is developed by CMRI Regional Centre and Wavelet Group of Pune, India. The photographs from the field are downloaded into the computer and processed for greyscale, image enhancement, calibration, and grain analysis. The software can determine the area, size, and shape of the fragments in a muckpile on the basis of greyscale difference. The 2D information available from software can further be processed for stereological analysis for 3D information (Venkatesh, 2010).

SPLIT System

The Split system was developed at the University of Arizona for measuring the size distribution of fragmented rock. The system divides two types of techniques. First, Split-Desktop analyzes photographs from the field. The other technique is Split-Online, which uses more than one camera installed on the conveyer or the crusher. Split-Desktop's steps are image taking, delineation, scaling, delineation editing, estimating fines, and calculating results. The scaling objects are used in measurement of fragmented rock size. Any shape of objects such as rulers or balls are located on the pile. Scaling requires at least one identifiable object of known size in the image. Split-Desktop allows one to three scales in each image. The delineation of fragmentation is a set of algorithms based on the following four steps: gradient filter, shadow convexity analysis, split algorithm, and watershed algorithm. Once the greyscale images have been completely edited, computation of size distribution can be carried out. In this step, the distribution of fines in each image can be calculated using two approaches Rosin-Rammler or Schuman distribution. The results are presented in graphical form and as tabulated text. The size distribution curve can be plotted as linear-linear plot, log-linear plot, and log-log plot. The most commonly used plot is log-linear plot. More than one image result can be plotted as combined at the same plot. Also the user can enter the proposed reference curve into the plot (Split-Desktop Manual, 2011).

Stereoscopic Analysis

In the early 1990s, Cheung and Ord attempted to measure the three-dimensional (3D) profile for rock fragmentation analysis using light stripes and a single camera. The most recently introduced image processing system components are a processing unit, stereo camera and software user interface.

This method uses 3D imaging to take images without the need for scaling reference objects. It can be applied for automatic rock size measurement from various sources, such as mining shovels, loaders, and crushers. The stereo camera produces depth information of each object in the scene by using binocular disparity. Using the triangulation method, the 3D positions of points in the image are calculated. The stereoscopic camera pair produces a rectified to the image of the scene as well as a 3D point cloud corresponding to the scene.

Images from the camera are corrected for distortion, then processed by a rock delineation algorithm to identify the boundaries of each particle in the image. For each set of boundary pixels, the algorithm identifies the corresponding points in the 3D point cloud. These coordinates are then used to calculate the sieve size for the rock, as well as to estimate its volume (Sameti, 2015).

Table 2.2 Comparison of image analysis systems (Maerz,1996, Haverman,1996, Kemeny,1994)

Systems	Proposed by	Used algorithms	Year
IPACS	Dahlhielm	Remove noise, curve surface thresholding, segmentation based on a 2x2 partition mode test, background splitting, region merging and pixel aggregation	1996
TUPICS	Havermann and Vogt	Edge detection, thresholding, custom contour closing, and object filling	1996
FRAGSCAN	Schleifer and Tessier	Local and global equalization, thresholding, and successive morphological openings.	1996
WIPFRAG	Maerz	Thresholdiong, gradient edge detection	1996
SPLIT	Kemeny	Greyscale equalization, Sobel edge detection, thresholding, watershed segmentation	1994
CIAS	Downs and Kettunen	Edge detection, segmentation algorithm	1996

Summary of image analysis systems

The image processing method determines particle sizes of fragmented rocks after blast in two dimensions using thresholding, Sobel edge detection algorithm, and watershed segmentation algorithms on digital images. Using technological advances, various software packages have been developed for image processing analyses.

The advantages of the image processing methods:

- Easy and simple to use
- Time efficient (in a matter of seconds)
- Low cost, less initial investment required
- Capable of automatic and continuous use
- Applicable to other industries, such as roads and construction
- Transferable to 3D image processing analysis using stereoscopic camera.

The disadvantages of image processing methods:

- Results of image processing method are directly influenced by many factors such as lighting, resolution, scaling, image taking orientation, and fines estimation.
- For validation, may require sieving analysis.

2.3 Rock Blasting Fragmentation Prediction

The Kuz-Ram model was developed by Cunningham (1983) for prediction of rock fragment size distribution. There are three main formulas and, in addition, Lilly (1986) developed a formula for rock factor.

The first effort in rock fragmentation prediction was made by Kuznetsov and Koshelev in 1973, when they experimentally investigated the Rosin-Rammler law using a wide range of materials, structures, and shapes. Kuznetsov (1973) developed a semi-empirical formula for the mean fragment size of the blasted rock based on rock properties and explosive properties.

The Kuznetsov's mean fragment size equation based upon ANFO can be written as:

$$X_m = A\left(\frac{V_0}{Q_e}\right)^{0.8} Q_e^{\frac{1}{6}} \left(\frac{S_{ANFO}}{115}\right)^{-19/30} \quad (2.6)$$

Where X_m – mean fragment size (cm)

Q_e – mass of explosive per blasthole (kg)

V_0 – rock volume (m^3)

S_{ANFO} – relative weight strength of the explosive to ANFO (ANFO =100)

A is the rock factor, its value is depending on rock hardness:

$$A = \begin{cases} 7 - for\ medium\ hard\ rock, f = 8 - 10 \\ 10 - for\ hard\ but\ highly\ fissured\ rocks, f = 10 - 14 \\ 13 - for\ very\ hard, weakly\ fissured\ rocks, f = 12 - 16 \end{cases}$$

The Rosin-Rammler formula (1933) is used to predict the fragment size distribution. It is generally recognized as giving a reasonable description of fragmentation in blasted rock. This equation is:

$$R_m = 1 - e^{-\left(\frac{X}{X_C}\right)^n} \quad (2.7)$$

where R_m - the proportion of material retained on the screen,

X - the screen size (cm)

X_C - the characteristic size (cm)

n - the uniformity index. The characteristic size X_C is one through which 63.2% of the particles pass. If the characteristic size X_C and the uniformity index n are known, a typical fragmentation curve can be plotted.

The value of the uniformity index determines the shape of the Rosin-Rammler curve. High values indicate uniform sizing. Low values, on the other hand, suggest a wide range of sizes including both oversize and fines. This combination of the Kuznetsov and Rosin—Rammler equation results in what has been called the Kuz-Ram fragmentation model (Hustrulid, 1999).

In 1986, Lilly developed a rock mass classification system, called the Blastability Index, which is based on four main rock mass parameters which contribute significantly to the performance of a blast:

- The structural nature of the rock mass, e.g. whether it is powdery, blocky or massive
- The spacing and orientation of planes of weakness such as joints, bedding planes schistosity and foliation
- The specific gravity of the material
- The hardness/strength of the material.

Structural Nature of the Rock Mass: If the rock is massive, the fragment size distribution will be almost entirely dependent on the generation and intersection of blast-induced fractures.

Joint Plane Spacing: In jointed rock masses, where fragment size and shape is dependent largely on the joints themselves, the spacing of existing planes of weakness will give the engineer a good idea of the size and shape of the fragments, which he will find in the muckpile after a blast. Rock masses containing closely spaced joint sets will require far lower energy factors than those where joint spacing is measured in meters.

Joint Plane Orientation: Horizontal planes of the weakness in a horizontal bench operation are a far easier proposition to blast than planes that are dipping in the direction of throw.

Specific Gravity and Hardness: these two parameters are much less important than other parameters. In general, heavier rock masses require more explosive energy to break and move than do lighter rocks. Harder rocks can be more difficult to break than softer rocks.

The parameters with their weighting factors are shown in following Table 2.3.

$$BI = 0.5\,(RMD + JPS + JPO + RDI + S) \qquad (2.8)$$

The various ratings are defined as follows:

Table 2.3 Ratings for blastability index parameters (Lilly, 1992)

Parameter		Rating
Rock Mass Description (RMD)		
	Powdery or friable	10
	Blocky	20
	Massive	50
Joint Plane Spacing (JPS)		
	Close (< 0.1m)	10
	Intermediate (0.1m to 1.0m)	20
	Wide (> 1.0m)	50
Joint Plane Orientation (JPO)		
	Horizontal	10
	Dip out of face	20
	Strike normal to face	30
	Dip into face	40

The rating for Rock Density Influence (RDI) is estimated as follows:

$$RDI = 25(D) - 50 \qquad (2.9)$$

Where D – the rock density (t/m^3)

Hardness was 1 to 10 (Lilly, 1986) then the formula is developed as H= 0.05 (UCS) (Lilly,1992)

The Blastability Index is adapted for Kuznetsov's model in attempting to better quantify the selection of rock factor "A." Cunningham (1987) stated the evaluation of rock factors for blasting should at least take into account the density, mechanical strength, elastic properties and structure. The equation of rock factor is:

$$A = 0.12\,BI = 0.06(RMD + JF + RDI + HF) \qquad (2.10)$$

The index of uniformity has been performed by Cunningham. He based his prediction of fragmentation on the Kuznetsov equation and used the relationship between fragmentation and

drilling pattern to calculate the blasting parameter of the Rosin–Rammler formula. The index of uniformity, n, is estimated by:

$$n = (2.2 - 14\frac{B}{D})\left(\frac{1}{2} + \frac{S}{2B}\right)^{0.5}(1 - \frac{W}{B})(\frac{L}{H}) \qquad (2.11)$$

where B - the burden (m)

S - the spacing (m)

D - the borehole diameter (mm)

W - the standard deviation of drilling accuracy (m)

L - the total charge length (m)

H - the bench height (m)

In the Kuz-Ram model, rock has been defined by a "Rock factor," which is recommended to be between 7 and 12, depending on the hardness and joining of the rock (Cunningham, 1983).

Limitations on Kuz-Ram model:

- The S/B ratio applies to the drilling, not the timing, layout and should not exceed 2
- Initiation and timing must be arranged so as to reasonably enhance fragmentation and avoid misfires or cut-offs
- The explosive should yield energy close to its calculated Relative Weight Strength
- The jointing and homogeneity of the ground require careful assessment, as fragmentation is built into the rock structure, especially when loose jointing is more closely spaced than the drilling pattern.

Chapter 3 Measurements and Analyses of Rock Fragment Size Distributions at the Erdenet Mine

Rock fragment size measurements were carried out at the Erdenet Mine and analyses were conducted for fragment size distribution determination and prediction. A total of seventy-two pictures of rock fragments in eleven blasting patterns were taken at the Erdenet Mine. Twenty-eight pictures were analyzed using Split-Desktop image processing program, excluding those taken at too sharp an angle, at a too far distance away, with poor focus or been too shadowy.

3.1 Geological Information

The Erdenet porphyry copper-molybdenum deposit is a part of Erdenet complex. Geological age of Permian and Early Triassic or Isotopic age of 226-245 Ma (megaannum or million years ago). This deposit consists of stockwork veinlets and veins of quartz, chalcopyrite, and molybdenite in or near the granodiorite porphyry of the Selenge Complex (Warren J.Nokleberg, 2010).

The .size of the stockwork at the surface is 2,800 m by 300 to 1300 m and the primary ore dimensions are 1,000 by 600 m. The deposit is related to intensive hydrothermal alteration of host rocks (Warren J.Nokleberg, 2010).

In the eastern part of the deposit, the porphyritic rock and alteration zone is cut by a central meridian fault. The northwest trending fault zone is important for the ore location process.

The main minerals in the oxide zone are malachite, azurite, cuprite, iron oxides, and native copper. A vertical zonation consists of (1) oxidized and leached ore (from 10 to 90 m thick); (2) secondary sulphide-enrichment zone; and (3) primary ore (to a depth 905 m). The thickness of the secondary sulphide zone is between 60m to 300m, that zone has 85 percent of the reserves, and Cu grade varies from 0.8% to 7.6% and Mo grade varies from 0.001% to 0.76%. Copper grade in primary ore decreases from the center of stockwork (0.4-0.5%) to the periphery (0.15-0.3%). Approximately 0.025% molybdenum grade occurs in the primary zone (Warren J.Nokleberg, 2010).

Within the deposit, several major trends of tectonic discontinuities are identified: northwestern, latitudinal, northeastern, and roughly N–S. In the north, the ore stockwork and its metasomatic halo are cut off by a system of faults of west–northwestern trend. The fault fissure dips at an angle of 60°-70° southward under the deposit. In the east, the granodiorite- porphyry stock and

ore stockwork are pared by the N–S-trending Central fault, adjoined in the north by an upthrust of a northwestern trend. The neighboring Central area is displaced along the Central fault 150 m southward, and 200 to 300 meters relative to the Erdenetiin- Ovoo deposit (Malyutin, 2007).

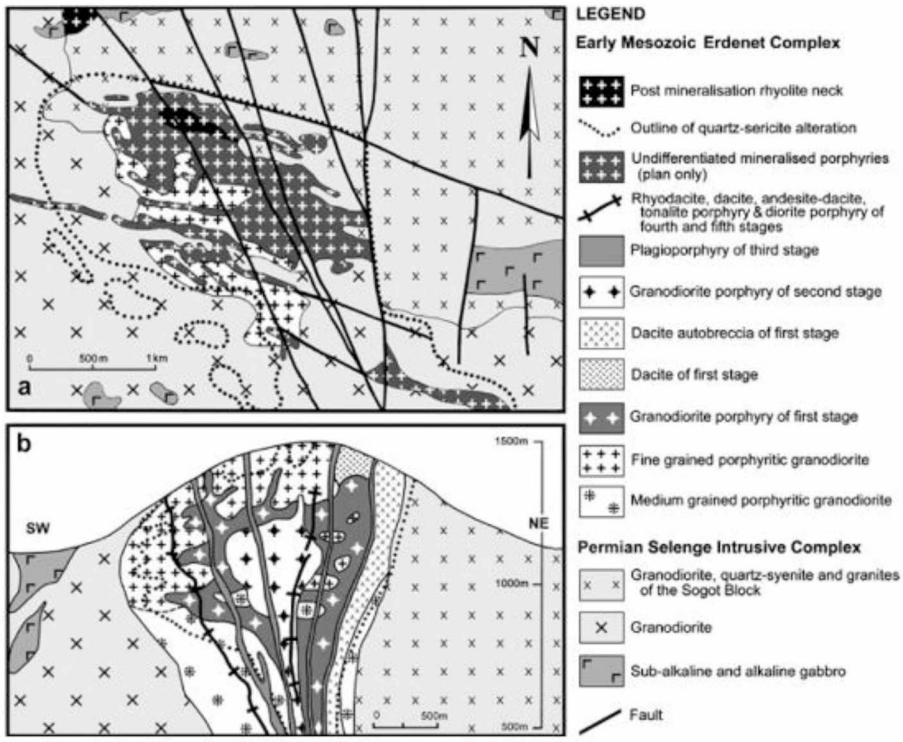

Figure 3.1 The geology and schematic structure of the Erdenet porphyry copper-molybdenum deposit a. Surface map and b. Schematic cross-section (Gerel and Munkhtsengel, 2005)

3.2 Image Sampling Analysis Using Split-Desktop

In this study, blast site data were collected from Erdenet Mine in Mongolia. Data from twenty-eight images of eleven blasts were obtained and image processing analyses were conducted.

Image processing analysis is divided into five steps: image taking, scaling, delineating, editing, and result generating.

3.2.1 Image Taking Process

A digital camera was used to take the images of the blasted muckpile,which were then analyzed using Split-Desktop. All of the images were well-focused. The image scaling is an important factor of getting image and rock fragments should be distinguishable in the image. The scales are: 1) large, 2) medium, and 3) small scales.

1) Large scale: The horizontal length of the image should be about 20 ft (7 m). These images can contain boulders, the coarse material or large areas of fines.
2) Medium scale: The horizontal length of the image should be about 8 ft (3 m). These images will provide a closer look at the medium size material. It has typical regions of 2 to 10 inch (5 to 25 cm) material.
3) Small scale: The horizontal length of the image should be about 1.5 ft (0.5 m). It is zoomed in images of representative samples of the finer material.

In this project, scales of images were all in medium scale.

For measuring material size in the Split-Desktop, scaling objects are used for reference. The scaling objects are known-sized objects of any kind, includes rulers, traffic cones or balls. Typically, one to three objects are allowed. In this study, two basketballs were placed near the top and bottom of each photographed area. The balls were placed on representative location of the all fragmented area that contains average sized of materials. The images were taken from five different positions and aimed at the same point. All images should be taken perpendicular to the line of the toe of the slope, using spherical objects (basketballs), to avoid skewing that may occur with non-spherical objects.

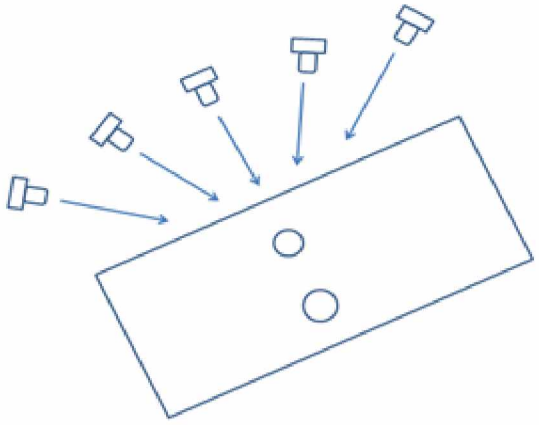

Figure 3.2 Image taking positions

Image lighting is also very important for image taking. If the image is too bright, shadows can make delineation difficult. If the picture is taken from too far away, it could cause causing too much waste area to be included in the picture, such as the sky and foreground, and the image cannot be analyzed properly. If one large rock covers an entire area, the image also cannot be analyzed.

The selected pictures in this study were appropriate for analysis.

Figure 3.3 Various picture samples: a) A picture taken too far away b) An acceptable picture (Slope angle clear, well-lit, and with few shadows) c) A unacceptable picture (as one large rock blocks entire area)

The resolution of the image should be sufficient, at least 1024x1024 pixels. Image sizes used in this study were approximately 2600 x 3800 pixels or 10MB. After the images were uploaded, the Split-Desktop automatically reduced resolution of images to 1700 x 1200 pixels or 2 MB.

3.2.2 Image Scaling Process

The scaling objects were used in this study to determine all fragment sizes. The scaling objects are known sized objects of any kind, which can be rulers, traffic cones or balls. One to three objects are allowed. In the study, two basketballs with a diameter 239.4 mm were placed near the top and bottom of each image area, as shown in Figure 3.4.

Figure 3.4 Muckpile image

Display of the scale length and the scale value was in pixels per unit (inch or mm). In the Split-Desktop image process, the scale was given manually for the first image and masking color (light blue) was placed on the balls. The subsequent images were then scaled automatically.

3.2.3 Delineation Process

Once the image is converted to digital form, it is processed using digital image processing routines with the final goal of image segmentation (Simphiwe, 2004). The first step of the process was to convert from the acquired images to greyscale images, as shown in Figure 3.5.

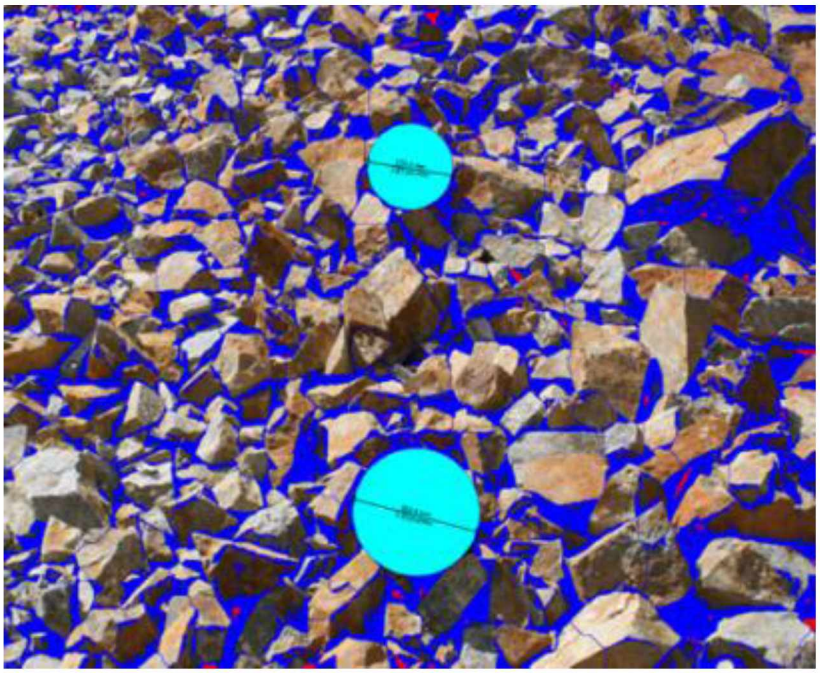

Figure 3.5 Greyscale image

A greyscale digital image is an image in which the value of each pixel is a single sample. The image color is shades of gray, varying from black at the weakest intensity to white at the strongest. The greyscale image gives an opportunity to use the algorithms for drawing edges.

A characteristic of fragmented rocks is the large percentage of the volume taken up by void space or porosity (10-40%). Under natural light, these void areas will appear as dark and shaded areas. These dark areas will partially outline the boundaries of the rock particles. In particular, where the shadow regions meet with particle edges, the shadow regions will form sharp convex shapes with angles that point in the direction of the edge between the touching particles (Ashutosh, 1992).

The delineation procedure is based on two algorithms. The first algorithm analyzes the shapes of shadow regions and searches for large gradient paths in the region ahead of sharp convexities in the shadow regions. Gradient value for a pixel is a measure of the contrast in grey level between the pixel and neighboring pixels. A high gradient value may indicate the presence of a boundary of a fragment (Ashutosh, 1992).

The basis for the algorithm1 is as follows:

1) The gradient values along the touching areas of particles are assumed to be larger than some threshold values.

2) The shadow boundary in the void space between particles tends to form convex regions that point in the direction of edges.
3) The rock particles under consideration are larger than some noise threshold.

The second algorithm is used to find clusters of undelineated touching particles whose gradient values along the touching areas are less than a prescribed gradient threshold value and delineate touching particles (Ashutosh, 1992).

The basis for the algorithm2 is as follows:

1) Cluster regions of touching particles are simply connected (they do not contain holes)
2) A cluster boundary at points where rock particles touch tends to form concave regions
3) The length between touching particles is relatively short compared with each individual particle perimeter on either side of the touching path.

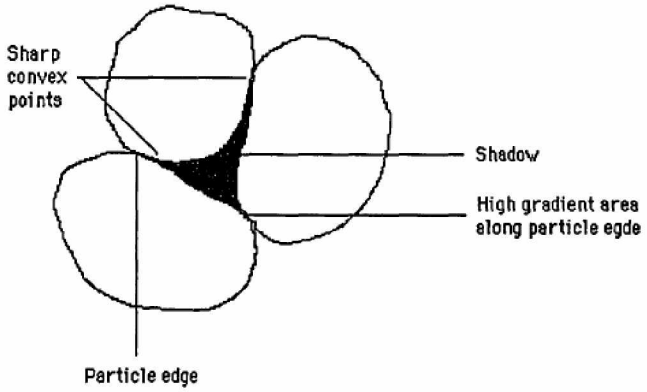

Figure 3.6 Delineating particles with gradient filter (Ashutosh,1992)

In the region where rock fragments touch, there usually will be a relatively large gray level difference due to particle edges (Ashutosh,1992).

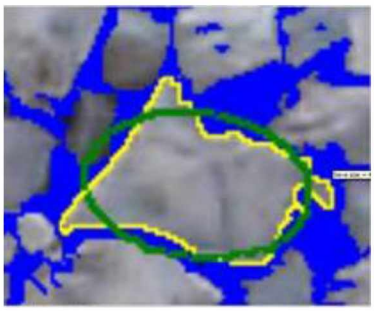

Figure 3.7 The best-fitting ellipse (Split-Desktop Manual, 2011)

After delineation, the fragments are calculated using the maximum area of the best-fitting ellipse.

3.2.4 Editing of the Delineation

After automatic delineation, the delineated area can be corrected manually. Manually editing involves three main operations: drawing boundaries, erasing, and filling particles with fines or masked colors.

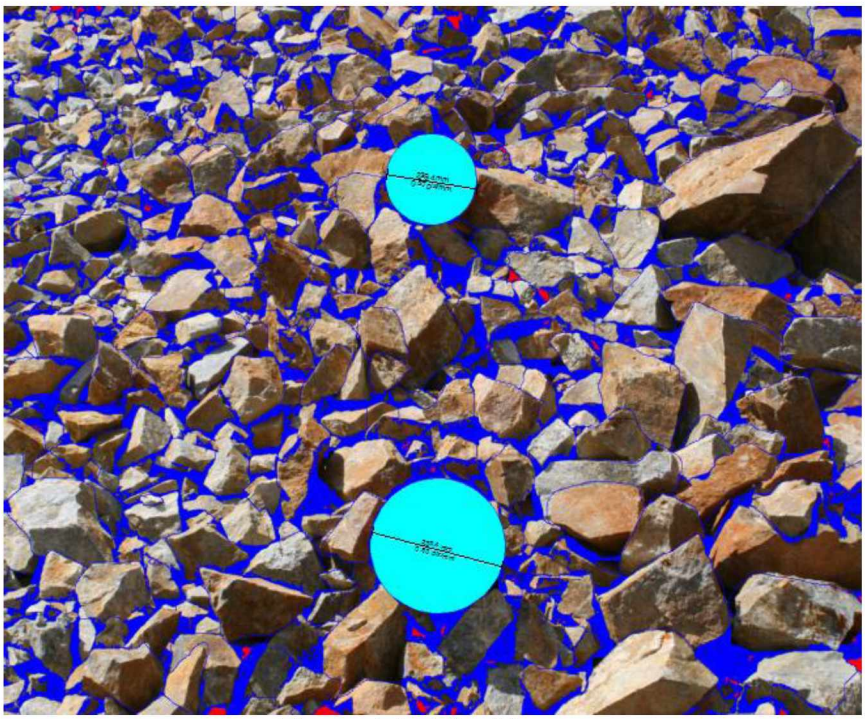

Figure 3.8 Edited image

The greyscale image allows for many different colors. In this case light blue for masking, dark blue for boundaries, and the red for fines. The masked area removes parts of the image from analysis by coloring; and these parts can be the scaling objects, sky, water or any other objects. Fine materials were colored in red.

Estimation of the size distribution: Once the greyscale images have been completely edited, computation of size distribution can be carried out. In this step, the distribution of fines in each image can be calculated using two approaches: Rosin-Rammler and Schuman distribution.

Estimation of fines factor is one of important part of size distribution calculation.

Split-Desktop can see and measure particles, but in every image there is a point below the resolution of the image where particles can no longer be seen and delineated. At this point, Split-

Desktop will estimate the remaining finer material. The "fines" cutoff basically depends on the resolution in pixel/unit of the image (Split-Desktop Manual, 2011).

Since the black pixels in the image represent both fines and outlines of particles, a percent of these pixels is included in the fines calculation. This percentage of black to be counted as fines varies for each muckpile and can be adjusted by the user. If we do not want any black pixels to count as fines, i.e. riprap material where the fines have been screened out, then select "Zero", which will enter 0% (Bobo, 2003). Based on percentage of fines material, the fines factor can be selected as very high, high, medium, low, or none. If the images are taken from the same muckpile, the fines factor should be chosen the same value.

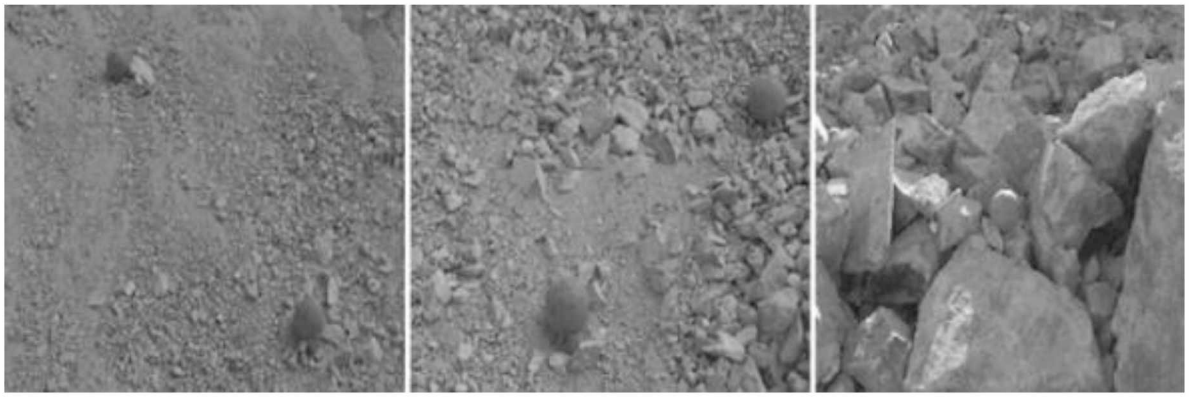

Figure 3.9 Example of Fines a) High or 80% -100% b) Medium or 50% c) Low or 10% -20%

In this case, the fines factors were mostly chosen as 20% and 50% of fines. The values of fines cutoff were determined from image pixels, which varied from 41mm to 137 mm.

3.2.5 Result Generating

Results are presented in graphical form and as tabulated text. The size distribution curve can be plotted as linear-linear plot, log-linear plot, and log-log plot. Most common used plot is log-linear plot. More than one image result can be plotted as combined with the same plot. Also, a user can enter the proposed reference curve into the plot.

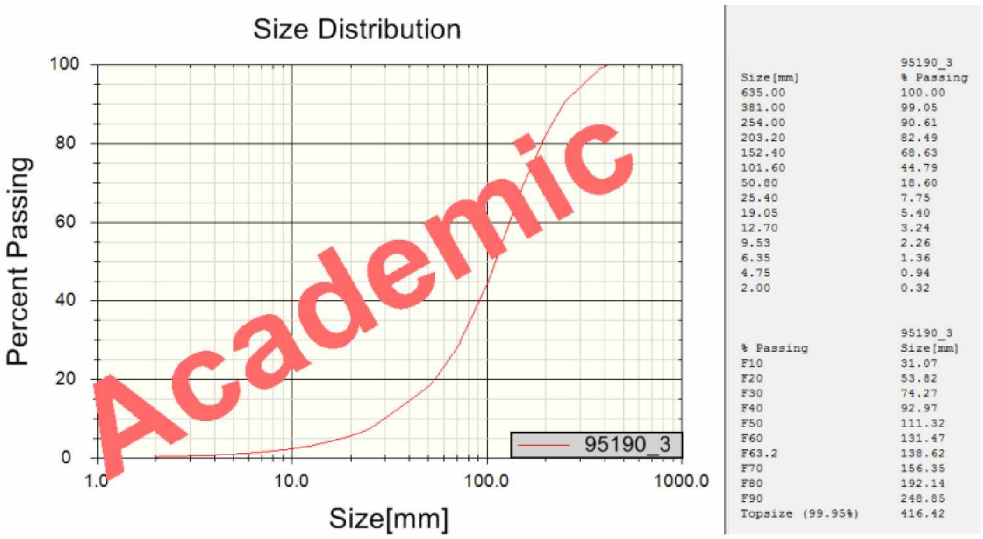

Size[mm]	95190_3 % Passing
635.00	100.00
381.00	99.05
254.00	90.61
203.20	82.49
152.40	68.63
101.60	44.79
50.80	18.60
25.40	7.75
19.05	5.40
12.70	3.24
9.53	2.26
6.35	1.36
4.75	0.94
2.00	0.32

% Passing	95190_3 Size[mm]
F10	31.07
F20	53.82
F30	74.27
F40	92.97
F50	111.32
F60	131.47
F63.2	138.62
F70	156.35
F80	192.14
F90	248.85
Topsize (99.95%)	416.42

Figure 3.10 The size distribution curve and results

One of the size distribution curves is shown in Figure 3.10. The user can enter and see his/her own passing percent or screen size. In this study passing percent of 63.2 % is additionally entered. Results were passing percent in percentage and screen size was in mm.

The measured fragment size for the Erdenet Mine are shown at mean size (P50), characteristic size (X_C or P63.2) and passing percent eighty (P80) in Table 3.1.

Table 3.1 Fragment size distribution at Erdenet Mine - results from Split-Desktop

	Pattern number	Uniformity Index, n	Mean Size, P50, (mm)	Characteristic Size, X_C (mm)	Passing Percent, P80, mm
1	70400	0.93	223.38	330.84	495.79
2	95175	1.27	188.92	252.25	356.50
3	65025	1.90	77.47	93.99	123.72
4	10263	1.13	102.29	141.49	211.79
5	25319	1.32	132.24	174.65	246.61
6	95190	1.55	105.84	134.13	188.96
7	30325	0.76	62.11	100.47	159.38
8	80101	1.74	56.93	70.29	91.95
9	80102	1.61	282.46	354.85	446.81
10	65022	1.58	198.61	250.39	331.68
11	45515	1.49	151.13	193.41	268.28
Minimum		0.76	56.93	70.29	91.95
Overall Average		1.39	143.76	190.61	265.59
Maximum		1.90	282.46	354.85	495.79
Standard Deviation		0.34	72.51	95.82	130.06

The uniformity index ranges from 0.76 to 1.9. The mean of the uniformity indices is 1.39, which is within the range suggested by Cunningham (1987).

The mean fragment sizes ranged between 56.93 mm and 282.46 mm. The overall average fragment size was 143.76 mm and standard deviation was 72.51 mm. Uniformity index was ranged 0.76 to 1.90 and average value was 1.39.

3.2.6 Comparison of the Size Distributions for Different Rock Types

3.2.6.1 Comparison of the Size Distributions for Different Rock Types

Protodyakonov's hardness factor is one of the main factors in the Erdenet Mine (Table A.2). For this reason, patterns were categorized into four different hardness factors, and the average values were calculated for each hardness factor.

For rock type with hardness factor of 12: Just one blasting pattern (70400) was measured during the study time. Rock strength was the weakest of study area and rock type was mostly granite and granodiorite. Four images were processed, and the overall mean size was 223.38 mm (Figure B.20 to B.24).

For rock type with hardness factor of 13: Six blasting patterns and 17 images were measured in this hardness factor (Figure B.1-B.12, B.19, and B.27-B.33). Various kinds of rocks were contained, including granite porphyry, fine-grained granodiorite, diorite and basaltic dykes.

The mean size of each type of rock ranged from 62.11 mm to 188.92 mm, and the overall average was found to be 111.48 mm.

For rock type with hardness factor of 14: Three patterns were measured, including three of the images (Figure B.18, B.25 and B.26). The mean sizes were measured from 56.93 mm to 282.46 mm, and average was 179.33 mm.

For rock type with hardness factor of 15: Only one blasting pattern was measured (Figure B.13-B.17). Rock strength was the strongest of study area and rock type was mostly trachydacite, trahi-riolit, and trahi-granite. Four images were processed, and mean size of each type of rock ranged from 62.11 mm to 188.92 mm, and the overall average was found to be 111.48 mm.

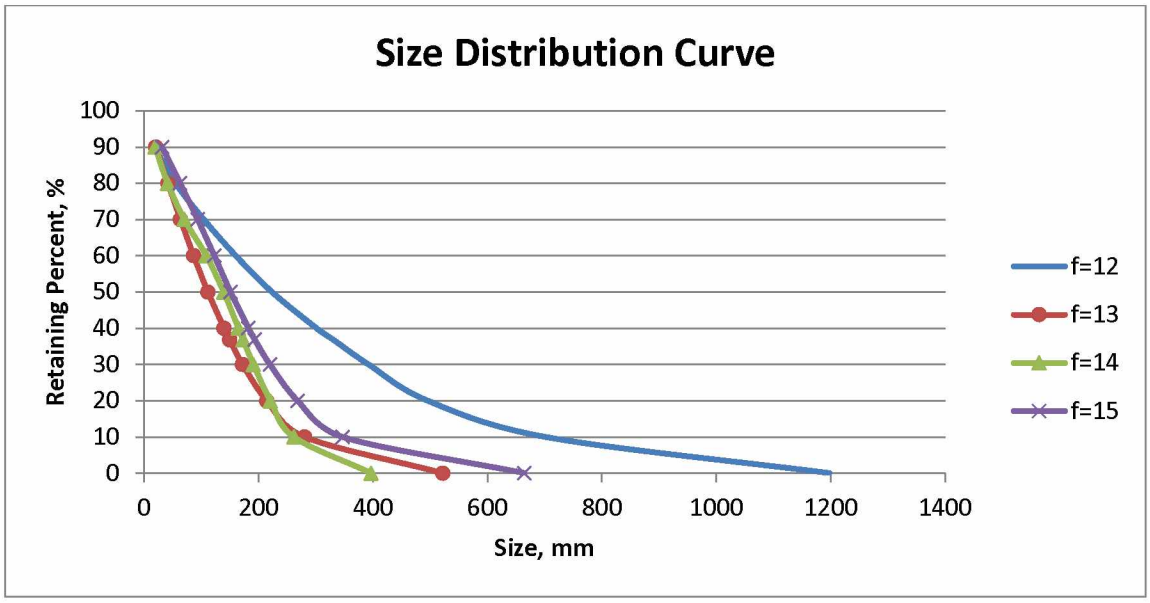

Figure 3.11 Comparison of size distribution curve of measured at different hardness factor

Average measured uniformity indices at hardness factor of 12, 13, 14 and 15 were 0.93, 1.25, 1.67 and 1.49 respectively. We can see the size distribution curve of 12 was more uniform than others, on the contrary, the curve of hardness factor of 14 is non-uniform distributed (Figure3.11).

3.2.6.2 A Comparison between the Rock Fragment Size Distribution Studies of Year 2014 and Year 2009

The size distribution measurement has been conducted in Erdenet Mine. Last measurement was conducted by other researchers (Nyamdorj, et al.) in 2009. The fragmented rock size distributions of the studies at hardness factor of 13 is presented in Figure 3.12.

According to the Erdenet open pit mine requirement, the passing percent at 600 mm of fragment size after blasting should be over 80 percent.

During test time the passing percentages at 400 mm and 600 mm were measured as 77.5% and 87.3% respectively.

In the current study, the passing percentages were 95.56% and 99.19%. The blasting quality has improved by 17.97% and 11.45%. All these results are tabulated in Table A.4.

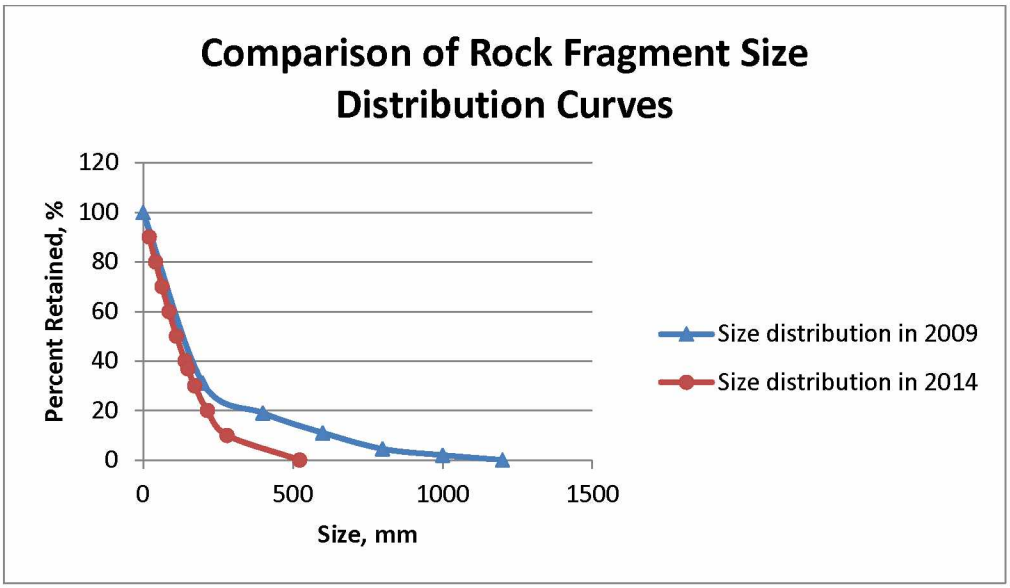

Figure 3.12 Measured size distributions in different study

3.3 Fragmentation Prediction Using the Kuz-Ram Model

A comprehensive rock mechanic test was conducted at Erdenet Mine in 2004. Nyamdorj and Laikhansuren (2004) determined the value of rock properties including the Protodyakonov's hardness factor for each kind of rock type. The results are presented in Table 3.2

Table 3.2 The average rock mechanic properties at the Erdenet Mine

Rock types	Protodyakonov's hardness factor	Compressive strength			Young's modulus		
		kgf/cm^2	psi	MPa	kgf/cm^2, 10^5	psi	GPa
Porphyritic granite	9	878	12494	86	6	8.19E+06	56
Granodiorite, medium-grained diorite to granodiorite	9	886	12600	87	8	1.08E+07	74
Medium-grained diorite to granodiorite	11	1132	16107	111	9	1.27E+07	88
Medium-grained diorite to granodiorite	12	1204	17119	118	8	1.13E+07	78
Fine-grained granodiorite	13	1275	18130	125	7	9.90E+06	68
Trachyte, andesite	15	1520	21622	149	8	1.08E+07	74
Fine-grained granodiorite	9	862	12263	85	6	8.19E+06	56
Medium-grained granodiorite	10	982	13963	96	6	8.65E+06	60
Biotite, porphyritic feldspar (dike)	14	1408	20021	138	10	1.48E+07	102

Based on the above study results, the compressive strength and Young's modulus were determined for each blasting pattern. The values of uniaxial compressive strength and Young's modulus were within the range of typical rock properties. The results are shown in Table 3.4.
The joint spacing is determined by rock types and fracture category provided by Laikhansuren on fracture categories at the National Mining Research Center-Sochinsky Institute of Mining in 1968 (Table 3.3).

Table 3.3 Fracture categories and joint spacing for various rock types at the Erdenet Mine

Rock Type	Fracture category	Joint Spacing, m
Fine-grained, biotite granodiorite	3	0.5
Fine-grained granodiorite with biotite porphyry	4	1
Medium-grained quartz-fluorite element	5	1-1.5
Dacite dyke contained granodiorite porphyry	4	1
Plagioclase and biotite phenocrysts	5	1
Fine-grained granodiorite	4	1-1.5
Fine-grained porphyry	3	0.5
Hornblende-biotite granodiorite (grano-syenite)	4	1
Quaternary rocks	3	0.5
Fine-grained, granodiorite porphyry	5	1.5

Based on the above categories, the joint spacings of blasting patterns were determined and are shown in Table 3.4.

Table 3.4 The joint spacing and rock properties for each blasting pattern

Blasting Pattern	Rock Types	Hardness factor	Fracture category	Joint Spacing, m	UCS, MPa	Young's Modulus, GPa
70400	Granite and granodiorite	12	3	0.5	118.03	78.06
95175	Fine-grained, biotite granodiorite	13	3	0.5	125.01	68.26
65025	Fine-grained granodiorite	13	4	1	125.01	68.26
10263	Granodiorite porphyry with fractures	13	4	1	125.01	68.26
25319	Granodiorite porphyry with fractures	13	4	1	125.01	68.26
95190	Granite porphyry and granodiorite porphyry with differently oriented fractures. Dykes with fractures containing syenite-diorite, diorite and basaltic	13	4	1	125.01	68.26
30325	Granodiorite	13	5	1.5	125.01	68.26
80101	Granite, granodiorite	14	4	1.2	131.99	58.45
80102	Granite, granodiorite	14	4	1.2	131.99	58.45
65022	Fine-grained granodiorite	14	3	0.5	131.99	58.45
45515	Trachydacite, trachyrhyolite, trachy-granite	15	3	0.5	149.09	74.14

The properties of explosives are shown in Table 3.5.

Table 3.5 Explosive properties

Type of Explosive	VOD, m/s	Density, kg/dm^3	Released heat, kcal/g
Emulsion	3400	1.3	900
ANFO(6% of FO, 94% of AN)	3000	0.9	850

The current blasting pattern design parameters are given below. The blast hole diameter was 250 mm, drilling accuracy was 0.45 m, bench height was 15 m, subdrilling was 2 m, hole pattern geometry was square and the other parameters are shown in Table 3.6. Delay timing of hole to hole and delay timing of row to row were 17 ms and 42 ms respectively.

Table 3.6 The blasting design parameters of the Erdenet Mine

	Pattern Number	Blasthole Condition	Blasthole Depth (l), m	Bench Height (H), m	Burden (B), m	Spacing (S), m	Amount of Explosive per Hole, kg	Powder Factor, kg/m^3	Charge Length (L), m
1	70400	dry	17.3	15.3	8.5	8.5	525.63	0.53	10.3
2	95175	wet	17.1	15.1	8	8	459.80	0.54	10.1
3	65025	wet	16.5	14.5	8	8	504.30	0.57	9.5
4	10263	wet	17.0	15.0	8.5	8.5	590.95	0.59	10.0
5	25319	wet	17.1	15.1	8.5	8.5	690.57	0.64	10.1
6	95190	wet	17.7	15.7	8.5	8.5	635.79	0.64	10.7
7	30325	wet	17.4	15.4	8.5	8.5	559.52	0.57	10.4
8	80101	wet	17.5	15.6	8	8	689.70	0.69	10.6
9	80102	wet	16.4	14.5	8.5	8.5	593.40	0.67	9.5
10	65022	wet	16.2	14.2	8.5	8.5	583.24	0.41	9.2
11	45515	wet	16.9	14.9	8.5	8.5	471.00	0.64	9.9

The values of rock factor, average fragment size, uniformity index, characteristic size, and size distribution curve were calculated using rock and explosive properties, and blasting parameters shown above.

The Rock Factor Calculations for Erdenet Mine

The rock factors were calculated by Lilly's formula. He described that the blastability index should be based on the structural nature of the rock mass, the spacing and orientation of joint planes, the specific gravity of the materials, and the rock strength.

Based on the observation and measurement, the rock mass is vertically jointed and block size was approximately measured as 0.5 m to 1.5 m. The rating of rock mass description was the same value as the joint factor.

The joint spacing was determined based on rock types and fracture categories provided by National Mining Research Center-Sochinsky Institute of Mining (Laikhansuren, 2000).

Using the above categories, the joint spacing of blasting patterns were determined and are shown in Table 3.4.

The joint plane angle is determined as approximately perpendicular to the bench face and the rating is 30.

Density of the ore and rock varies from 2.5 to 2.7 t/m^3. In this project, the average rock density was 2.6 t/m^3.

Young's modulus and uniaxial compressive strength were obtained from a previous study (Nyamdorj, 2009). The values of Young's modulus of the blasting patterns were greater than 50 GPa, therefore the rating of the hardness factor is estimated based on uniaxial compressive strength. The uniaxial compressive strength values are within range of the typical rock properties.

The estimated rock factor is within the suggested range by Cunningham (1987), the summary of the estimation is in Table 3.7.

Table 3.7 Results of the rock factor calculation

Pattern number	Joint Spacing, m	UCS, MPa	Young's Modulus, GPa	RMD, Powdery/ Friable	JPS Vertical Joint Spacing, 0.1~MS	JPA, Strike Perp. to Face	Rock density, t/m^3	RDI, t/m2	Y>50 GPa UCS/5	Rock Factor, A
70400	0.5	118.03	78.06	10	20	30	2.6	15	23.61	5.92
95175	0.5	125.01	68.26	10	20	30	2.6	15	25.00	6.00
65025	1	125.01	68.26	10	20	30	2.6	15	25.00	6.00
10263	1	125.01	68.26	10	20	30	2.6	15	25.00	6.00
25319	1	125.01	68.26	10	20	30	2.6	15	25.00	6.00
95190	1	125.01	68.26	10	20	30	2.6	15	25.00	6.00
30325	1.5	125.01	68.26	10	50	30	2.6	15	25.00	7.80
80101	1.2	131.99	58.45	10	50	30	2.6	15	26.40	7.88
80102	1.2	131.99	58.45	10	50	30	2.6	15	26.40	7.88
65022	0.5	131.99	58.45	10	20	30	2.6	15	26.40	6.08
45515	0.5	149.09	74.14	10	20	30	2.6	15	29.82	6.29

Example calculation for Blasting pattern 95190 can be shown as:

Here RMD is 10 (friable), JPS is more than 0.1 m, and the rating is 20, JPA is 30, rock density is 2.6 t/m^3,Young's modulus is more than 68.26 GPa and UCS is 125.01 MPa. These values are tabulated in Table 3.7. The RDI is calculated as:

$$RDI = 25 * \rho - 50 = 25 * 2.6 - 50 = 15$$

$$S = \frac{UCS}{5} = \frac{125.01}{5} = 25$$

The rock factor A is calculated by Lilly's formula (Equation 2.8).

$$A = 0.12 * BI = 0.06\,(RMD + JPS + JPO + RDI + S)$$

$$A = 0.06\,(10 + 20 + 30 + 15 + 25) = 6$$

The mean fragment size was calculated by Kuznetsov's equation (Equaion2.6);

$$X_m = A\left(\frac{V_0}{Q_e}\right)^{0.8} Q_e^{\frac{1}{6}} \left(\frac{S_{ANFO}}{115}\right)^{-19/30}$$

Where, V_0 = rock volume = H*B*S = 15.7 * 8.5 * 8.5 = 1134.32 m^3

Q_e = mass of explosive per blasthole = 635.79 kg

S_{ANFO} = relative weight strength of the explosive to ANFO = 100

$$X_m = 6\left(\frac{1134.32}{635.79}\right)^{0.8} (635.79)^{\frac{1}{6}} \left(\frac{100}{115}\right)^{-\frac{19}{30}} = 30.54\,cm$$

The uniformity index was estimated by Cunningham's formula (Equation, 2.11).

$$n = (2.2 - 14\frac{B}{D})\left(\frac{1}{2} + \frac{S}{2B}\right)^{0.5} (1 - \frac{W}{B})(\frac{L}{H})$$

Where, B = burden = 8.5 m

S = the spacing = 8.5 m

D = the borehole diameter = 250 mm

W = the standard deviation of drilling accuracy = 0.45 m

L = the total charge length = 10.7 m

H - the bench height = 15.7 m. These information are tabulated in Table 3.6.

$$n = \left(2.2 - 14\,\frac{8.5}{250}\right)\left(\frac{1}{2} + \frac{8.5}{2\,(8.5)}\right)^{0.5}\left(1 - \frac{0.45}{8.5}\right)\left(\frac{10.7}{15.7}\right) = 1.11$$

All these results are in Table 3.9. Using the Rosin-Rammler equation (Equation 2.7), the characteristic size was calculated and the rock fragment size distribution curve was plotted.

$$R_m = 1 - e^{-(\frac{X}{X_C})^n}$$

Where R_m is the proportion of material passing the screen, X is the screen size in cm, X_C is the characteristic size in cm, and n is the uniformity index. If the screen size is given from 0 to 100 cm, the passing percent or retained percent can be calculated with Equation 2.7. The rock fragment size distribution curve was graphed and compared with image processing results for the Blasting pattern 95190 in Figure 3.14.

The size distribution curve of the Kuz-Ram model was more smoothly and uniformly distributed than curve of image processing. If we compare the overall average value of the mean sizes of image processing with the Kuz-Ram model, the values are 143.76 mm and 284.05 mm for the Blasting pattern 95190.

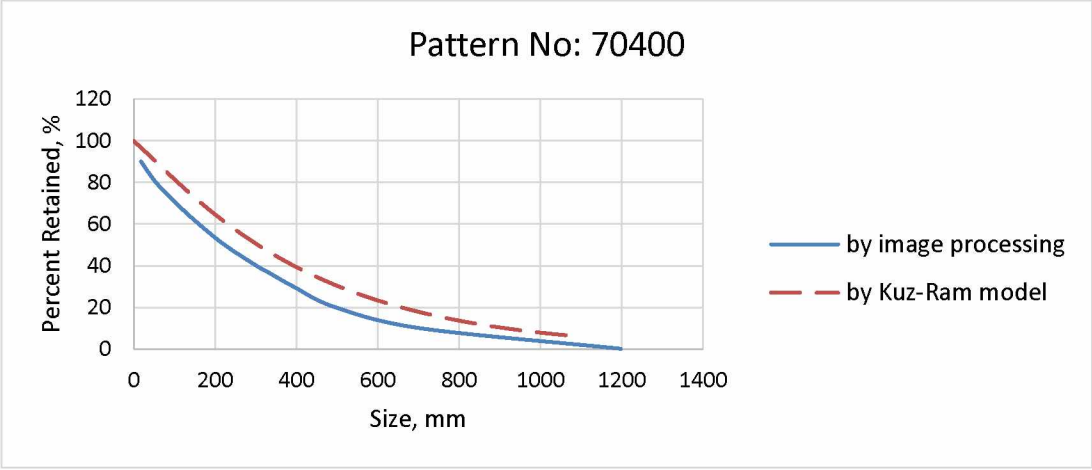

Figure 3.13 A comparison of the size distributions between image processing and the Kuz-Ram model for rock hardness of 12

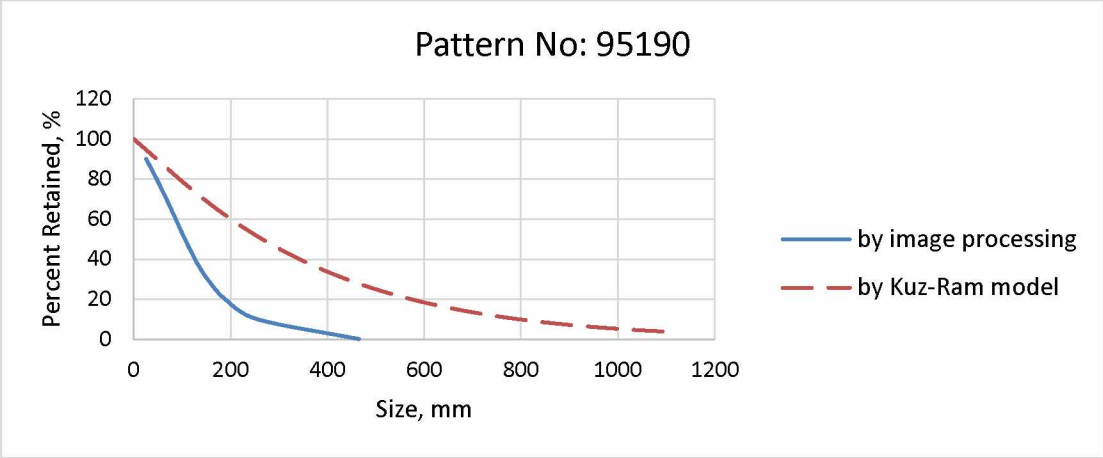

Figure 3.14 A comparison of the size distributions between image processing and the Kuz-Ram model for rock hardness of 13

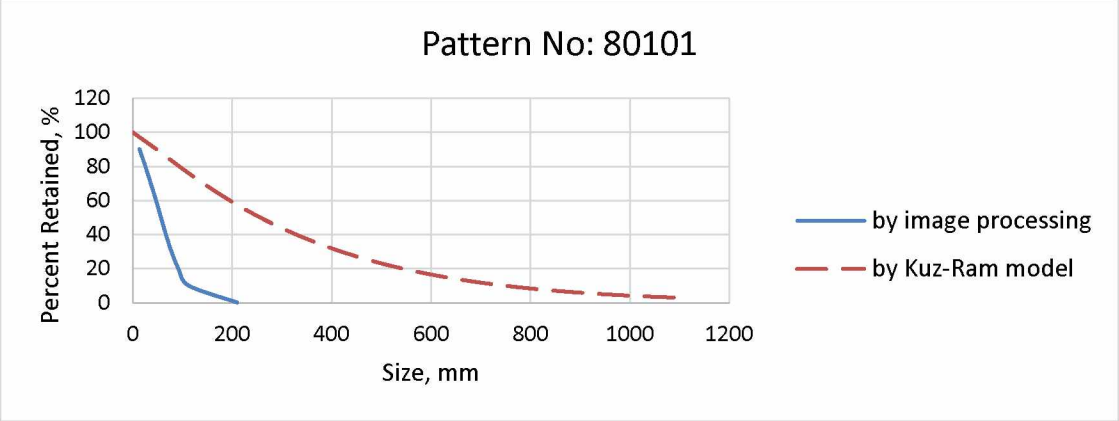

Figure 3.15 A comparison of the size distributions between image processing and the Kuz-Ram model for rock hardness of 14

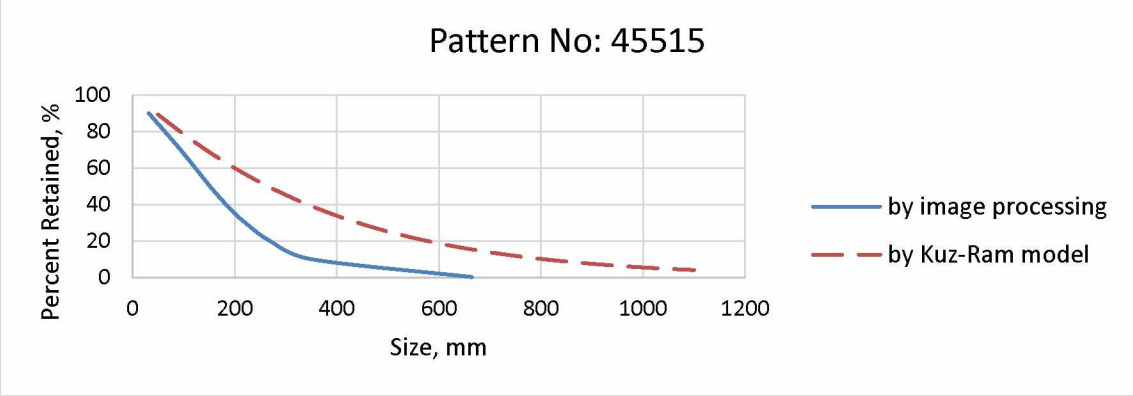

Figure 3.16 A comparison of the size distributions between image processing and the Kuz-Ram model for rock hardness of 15

Table 3.8 Comparison of the uniformity indices and the mean sizes between image processing and the Kuz-Ram model

Patterns	Hardness Factor	The Image Processing		The Kuz-Ram	
		Uniformity Index	Mean Size, mm	Uniformity Index	Mean Size, mm
70400	12	0.93	223.38	1.11	305.16
95190	13	1.55	105.84	1.11	264.95
80101	14	1.74	56.93	1.13	256.41
45515	15	1.49	151.13	1.10	264.16

These four graphs show the comparisons of the rock fragment size distributions of image processing and the Kuz-Ram model for different rock types. The rock types were granite and granodiorite for Pattern70400, granite porphyry and granodiorite porphyry for Pattern95190, granite and granodiorite for Pattern80101, and trahidacite, and trahi-granite for Pattern45515.

The measured value of Pattern80101 by image processing was with the smallest size of rock and more non-uniform compared to others. Otherwise, the fragment size Pattern70400 was closer in sizethe size of the Kuz-Ram model and the size distribution curve was very smooth.

The measured fragment size at P50, P63.2, and P80, and calculated uniformity indices are shown in Table 3.9.

Table 3.9 The results of the Kuz-Ram model

	Pattern number	Uniformity Index, n	Mean Size, P50, (mm)	Characteristic Size, X_C (mm)	Passing Percent, P80, mm
1	70400	1.11	305.16	426.01	657.21
2	95175	1.12	287.56	400.63	616.80
3	65025	1.09	279.66	392.33	609.25
4	10263	1.10	279.34	391.25	606.15
5	25319	1.12	268.62	374.24	576.38
6	95190	1.11	264.95	370.21	572.34
7	30325	1.11	284.55	396.83	611.59
8	80101	1.13	256.41	355.38	543.28
9	80102	1.08	256.02	360.71	563.52
10	65022	1.07	378.14	534.83	839.09
11	45515	1.10	264.16	370.41	575.28
Minimum		1.07	256.02	355.38	543.28
Overall average		1.10	284.05	397.53	615.54
Maximum		1.13	378.14	534.83	839.09

The uniformity index ranges from 1.07 to 1.13, and the mean value is 1.10.

3.4 Multivariate Nonlinear Regression Analysis of Fragment Size Distribution

The uniformity index and the characteristic size are the most important parameters in the determination of rock fragment size distribution. Therefore, we performed the statistical analyses of these two parameters in relationship with a number of variables in rock blasting.

In the regression analysis, the measured uniformity index and fragmented rock characteristic size were determined with the image processing method as presented in Section 3.2. A number of variables were also acquired for the analysis. The Young's modulus and the uniaxial compressive strength were determined previously by various researchers for the rock materials at the mine site. The explosive energy, bench height, burden, and spacing for the current rock blasting operations were also collected for the regression analysis.

3.4.1 Prediction Model Building for Rock Fragment Characteristic Size

Multivariate regression analysis is one of the most widely used of all statistical methods. A regression model contains one response variable and a number of predictor variables. In this case, the response variable was the "characteristic size" and four predictor variables were considered, including Young's modulus, uniaxial compressive strength, energy per unit volume, and bench height to burden ratio. The predictor variables can be first order or second order terms, interaction terms, and dummy variables. First, we can check the correlation between the variables and what kind of transformations are needed for response or predictor variables.

The following methods can be used to select the most important variables that contribute to the response variable. The most commonly used methods are: 1) Backward elimination method, 2) AIC based stepwise elimination, 3) F test criterion and 4) Adjusted R-squared method.

Backward elimination method: Start with all independent variables in the model, eliminate them one at a time. Using t-test, if p-value is greater than 0.05, eliminate the one with the highest value. This process will continue until all p-values are less than 0.05.

AIC based stepwise elimination: Akaike's information criterion is another known model selection criterion. Drop a variable at the condition that when it is dropped, making AIC lowest. If dropping a variable always raises AIC, we should stop the elimination.

F test criterion: The test statistic has an F-distribution under the null hypothesis. The sums of squares should be statistically independent.

Adjusted R-squared method: The method finds subsets of independent variables that best predict a dependent variable by linear regression in the given sample. Adjusted R-squared always identifies the model with the largest R-squared for each number of variables considered.

Table 3.10 Model variables for the fragment characteristic size

	Blasting Pattern	Characteristic Size,X_C, mm	Young's Modulus E, GPa	Uniaxial Compressive Stress,σ.c, MPa	Energy/Volume, kcal/m^3	Bench Height/Burden, H/B
		y	x_1	x_2	x_3	x_4
1	70400	330.84	78.06	118.03	404.17	1.80
2	95175	252.25	68.26	125.01	428.21	1.89
3	65025	93.99	68.26	125.01	489.08	1.81
4	10263	141.49	68.26	125.01	490.76	1.76
5	25319	174.65	68.26	125.01	569.68	1.78
6	95190	134.13	68.26	125.01	504.45	1.85
7	30325	100.47	68.26	125.01	452.58	1.81
8	80101	70.29	58.45	131.99	621.72	1.95
9	80102	354.85	58.45	131.99	509.78	1.71
10	65022	250.39	58.45	131.99	511.64	1.67
11	45515	193.41	74.14	149.09	393.77	1.75

In statistical terms, the relationship between variables is denoted by the correlation coefficient, which is a number between 0 and 1.0. Pearson's "*r*" is the most commonly applied correlation coefficient. The main ideas discussed here are similar for all correlation coefficients. The strength of relationship between variables is categorized in Table 3.11.

Table 3.11 Strength of correlation

Value of the Correlation Co-Efficient	Strength of the Correlation
1	Perfect
0.8-0.9	Very Strong
0.5-0.8	Strong
0.3-0.5	Moderate
0.1-0.3	Modest
>0.1	Weak
0	Zero

	y	x1	x2	x3	x4
y	1.00000000	0.06146501	-0.02442905	-0.39878180	-0.4953212
x1	0.06146501	1.00000000	-0.16651547	-0.72149925	0.0731903
x2	-0.02442905	-0.16651547	1.00000000	-0.08414379	-0.2555144
x3	-0.39878180	-0.72149925	-0.08414379	1.00000000	0.2423193
x4	-0.49532119	0.07319030	-0.25551440	0.24231925	1.0000000

Figure 3.17 Correlation matrix for fragment characteristic size prediction variables

We can predict the relationship between the rock fragment characteristic size (response variable) and the other variables (predictor variables). The rock fragment characteristic size appears to be moderately related to "energy per volume" and "ratio of bench height to burden." Young's modulus was strongly related to "energy per volume." UCS was modestly related to "Young's modulus" and "ratio of bench height to burden." "Ratio of bench height to burden" was related to all variables except "Young's modulus."

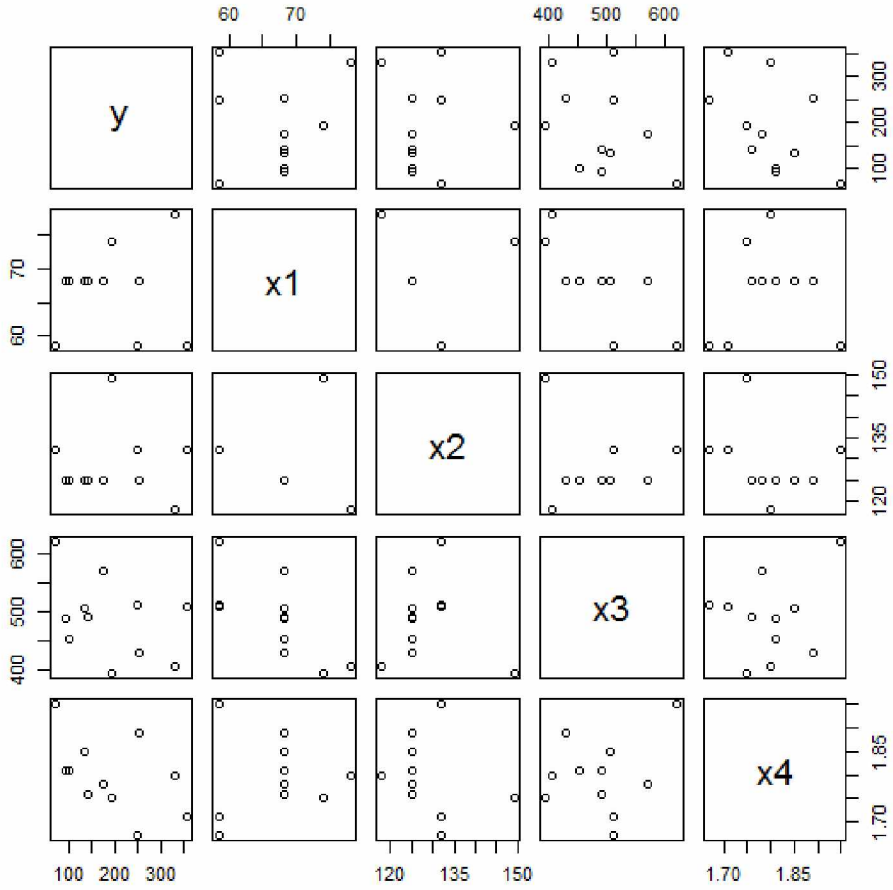

Figure 3.18 Scatter plot matrix for fragment characteristic size prediction variables

Scatter plots of the response variable (characteristic size) against each predictor variable are presented in Figure 3.18. This is helpful for studying the bivariate relationships among the predictor variables and for finding gaps and detecting outliers.

In this scatter plot, there is a correlation between the characteristic size and the ratio of bench height to burden because the plot looks like a line. Also, the similar shape of the line indicates correlation between "Young's modulus" and "ratio of energy to volume."

The Box-Cox procedure examines any transformation, needed or not, for the response variable. The procedure automatically identifies a transformation from family of power transformations of Y. The family of power transformations is of the form of $Y' = Y^{\lambda}$. The λ is called the power parameter (Kutner et al.,2004).

Table 3.12 Common Box-Cox Transformations

Lambda	Transformation
-2	$\frac{1}{y^2}$
-1	$\frac{1}{y}$
-0.5	$\frac{1}{\sqrt{y}}$
0	$log(y)$
0.5	$\sqrt{y}$
1	y
2	y^2

The common Box-Cox transformations for the response variable are tabulated in Table 3.12.

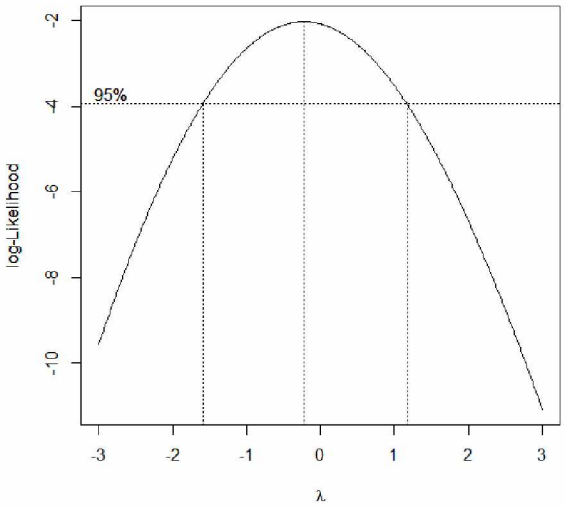

Figure 3.19 The Box-Cox result for the characteristic size prediction variables

The Box-Cox transformation offers a possible way for choosing a transformation of the response. The Box-Cox normality plot shows that the maximum value of the correlation coefficient is at λ=-0.2, which is near zero. If lambda equals zero, in this case the logarithmic transformation appears to be necessary for the model based on the Box-Cox plot. The R program was used for the regression model development and analysis. R is a free, open source programming language and software environment for statistical computing and graphics. Four types of elimination methods are used for model creating. After the elimination procedure, the created models are:

1. Backward elimination $\ln(y) = \beta_0 + \beta_1 x_1 + \beta_2 x_2 + \beta_3 x_3 + \beta_4 x_4 + \beta_5 x_1 x_2 + \beta_6 x_3 x_4 + \varepsilon_i$
2. AIC based stepwise elimination
   $\ln(y) = \beta_0 + \beta_1 x_1 + \beta_2 x_2 + \beta_3 x_3 + \beta_4 x_4 + \beta_5 x_1 x_2 + \beta_6 x_1 x_3 + \beta_7 x_1 x_4 + \beta_8 x_3 x_4 + \varepsilon_i$
3. F test criterion $\ln(y) = \beta_0 + \beta_1 x_1 + \beta_2 x_2 + \beta_3 x_3 + \beta_4 x_4 + \beta_5 x_1 x_2 + \beta_6 x_1 x_3 + \beta_7 x_1 x_4 + \beta_8 x_3 x_4 + \varepsilon_i$
4. Adjusted R-squared criterion $\ln(y) = \beta_0 + \beta_1 x_1 + \beta_2 x_2 + \beta_3 x_3 + \beta_4 x_4 + \beta_5 x_1 x_2 + \beta_6 x_3 x_4 + \varepsilon_i$

Two different models are created. Before doing the diagnostics the models are checked and compared. The models of the backward elimination and adjusted R-squared are same. In the t-test all p-values are significant and the overall p-value is 0.0359, which is less than 0.05, and adjusted R-squared is calculated as $R^2_{adj} = 0.7955$. The summary of the model is shown in Figure 3.20. The second model was created from the AIC based stepwise elimination and F test criterion. In the t-test all p-values are not significant and the overall p-value is 0.1848 and adjusted R-squared is calculated as $R^2_{adj} = 0.751$. The summary of the model is shown in Figure3.21.

The second model was not statistically significant; therefore, the best model was only the first model. The residual standard error of the first model was less than the residual standard error of the second one.

```
Call:
lm(formula = log(y) ~ x1 + x2 + x3 + x4 + x1 * x2 + x3 * x4)

Residuals:
         1          2          3          4          5          6
 7.445e-16  6.274e-02 -2.546e-01  2.898e-01 -1.170e-02  1.878e-02
         7          8          9         10         11
-1.050e-01  4.416e-03  1.783e-01 -1.827e-01  7.360e-17

Coefficients:
             Estimate Std. Error t value Pr(>|t|)
(Intercept) -2.687e+02  6.236e+01  -4.309   0.0126 *
x1           2.153e+00  4.794e-01   4.492   0.0109 *
x2           1.244e+00  2.759e-01   4.510   0.0107 *
x3           2.141e-01  5.593e-02   3.827   0.0187 *
x4           6.021e+01  1.617e+01   3.723   0.0204 *
x1:x2       -1.630e-02  3.599e-03  -4.530   0.0106 *
x3:x4       -1.170e-01  3.000e-02  -3.900   0.0175 *
---
Signif. codes:  0 '***' 0.001 '**' 0.01 '*' 0.05 '.' 0.1 ' ' 1

Residual standard error: 0.2395 on 4 degrees of freedom
Multiple R-squared:  0.9182,    Adjusted R-squared:  0.7955
F-statistic: 7.483 on 6 and 4 DF,  p-value: 0.03591
```

Figure 3.20 Summary of the model of Backward elimination

```
Call:
lm(formula = log(y) ~ x1 + x2 + x3 + x4 + x1 * x2 + x1 * x3 +
    x1 * x4 + x3 * x4)

Residuals:
         1          2          3          4          5          6
 7.302e-16  4.111e-02 -2.340e-01  2.145e-01 -5.310e-02  1.460e-01
         7          8          9         10         11
-1.145e-01  1.067e-16 -3.425e-15  4.048e-15  3.385e-17

Coefficients:
             Estimate Std. Error t value Pr(>|t|)
(Intercept) -5.515e+02  2.680e+02  -2.058    0.176
x1           5.769e+00  3.517e+00   1.640    0.243
x2           2.587e+00  1.739e+00   1.488    0.275
x3           1.637e-01  2.198e-01   0.745    0.534
x4           1.493e+02  8.287e+01   1.802    0.213
x1:x2       -3.438e-02  2.332e-02  -1.474    0.278
x1:x3        1.509e-03  2.197e-03   0.687    0.563
x1:x4       -1.121e+00  9.896e-01  -1.133    0.375
x3:x4       -1.465e-01  6.438e-02  -2.276    0.151

Residual standard error: 0.2643 on 2 degrees of freedom
Multiple R-squared:  0.9502,    Adjusted R-squared:  0.751
F-statistic: 4.769 on 8 and 2 DF,  p-value: 0.1848
```

Figure 3.21 Summary of the model of AIC based stepwise elimination

Now the diagnostic can be performed as in the following.

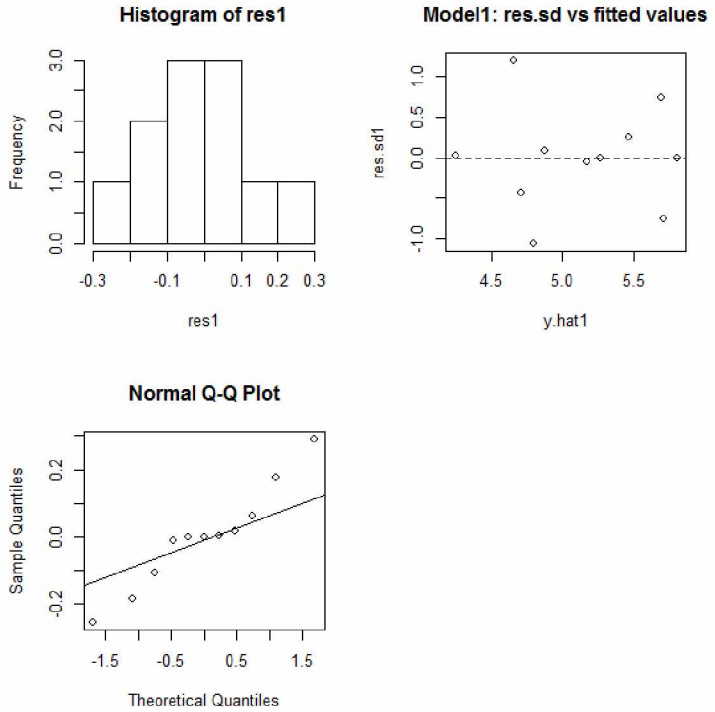

Figure 3.22 Histogram of residual, qq plot for diagnostics of the characteristic size model

The histogram is well shaped. On the residual plot, all points are inside of ±1.5 standard deviations. Normal qq plot is too skewed, which means residuals are not normally distributed. Usually the data set contains some cases that are outlying or extreme. These outlying cases may involve large residuals and often have dramatic effects on the fitted regression function. Therefore, it is important to study the outlying cases and to decide whether we should eliminate or retain them. The outliers were checked with hat matrix, standardized residuals and three dimensional scatter plot methods.

In this case the outliers were identified as the blasting patterns of 70400 and 45515. These patterns had the lowest and highest strength rocks.

```
Influence measures of
        lm(formula = log(y) ~ x1 + x2 + x3 + x4 + x1 * x2 + x3 * x4) :

      dfb.1_    dfb.x1  dfb.x2   dfb.x3  dfb.x4 dfb.x1.2 dfb.x3.4   dffit    cov.r  cook.d   hat inf
1   0.000000  0.00000  0.0000  0.00000  0.0000  0.00000  0.00000     NaN      NaN     NaN 1.000
2  -0.660576  0.34533  0.3864  0.86631  0.9577 -0.36559 -0.90052  1.6429 2.14e+01 0.44983 0.863   *
3  -0.374930  0.41883  0.4258  0.26030  0.2632 -0.42256 -0.26094 -0.6418 4.42e-01 0.05073 0.201
4   1.782343 -1.70123 -1.7454 -1.53338 -1.5998  1.71457  1.54571  2.2282 6.13e-03 0.31435 0.452   *
5   0.121446 -0.07454 -0.0708 -0.16582 -0.1496  0.06527  0.15861 -0.3102 5.68e+01 0.01825 0.872   *
6  -0.000471 -0.00626 -0.0063  0.00767  0.0081  0.00674 -0.00751  0.0377 9.21e+00 0.00027 0.198   *
7  -0.342750  0.33678  0.3382  0.29801  0.2882 -0.33156 -0.29221 -0.4442 7.06e+00 0.03446 0.421   *
8   0.019749  0.08554  0.0887 -0.17272 -0.1475 -0.09224  0.18043  0.8421 3.86e+02 0.13446 0.981   *
9  -0.267567  0.30101  0.3202  0.20825  0.1978 -0.32409 -0.21651  0.9599 1.71e+00 0.12991 0.467
10  0.159360 -0.23417 -0.2500 -0.09696 -0.0577  0.25928  0.10261 -1.3034 1.11e+00 0.21995 0.546
11  0.000000  0.00000  0.0000  0.00000  0.0000  0.00000  0.00000     NaN      NaN     NaN 1.000
```

Figure 3.23 Diagnostics for influential outliers in the model of characteristic size

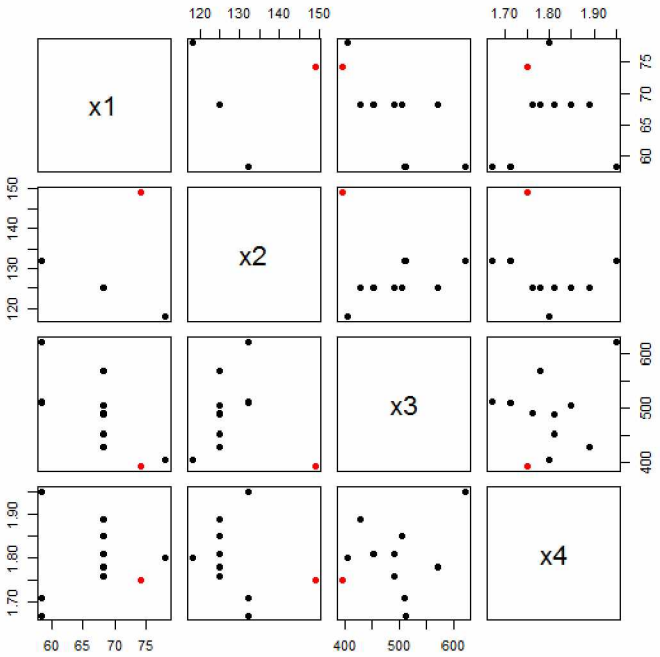

Figure 3.24 Three-dimensional scatter plot for the model of characteristic size

The predictor variables included in the model were sometimes uncorrelated to each other. The multicollinearity was investigated to check this correlation. A formal method of detecting the presence of multicollinearity that is widely accepted is the use of variance inflation factors. For the project, all four variance inflation factors for each predictor variable are calculated and the results do not exceed the limitation of 10, indicating that serious multicollinearity problems do not exist. Based on the diagnostics, the best model is chosen as follows:

$$\ln(X_C) = -268.7 + 2.153E + 1.244\sigma_c + 0.214(\frac{En}{V}) + 60.21(\frac{H}{B}) - 0.016(E * \sigma_c) - 0.117(\frac{En}{V})(\frac{H}{B})$$

This model can be expressed as:

$$X_C = e^{-268.7+2.153E+1.244\sigma_c+0.214\left(\frac{En}{V}\right)+60.21\left(\frac{H}{B}\right)-0.016(E*\sigma_c)-0.117\left(\frac{En}{V}\right)\left(\frac{H}{B}\right)} \qquad (3.1)$$

The outliers are not eliminated, because of the different types of rocks. Now we need a model for the uniformity index, then we will be able to predict the rock fragment size distribution.

3.4.2 Prediction Model Building for the Uniformity Index

In this case, the response variable was the uniformity index. Five predictor variables were considered, including Young's modulus, uniaxial compressive strength, energy per unit volume, bench height to burden ratio, and area per blasthole. The original values of the variables are shown in Table 3.13.

Table 3.13 Modelling variables of the uniformity index

	Blasting Pattern	Uniformity Index,n	Young's Modulus, E, GPa	Uniaxial Compressive Strength, σ.c, MPa	Energy/Volume, kcal/m^3	Bench Height/Burden, H/B	Area per Blasthole, BxS
		y	x_1	x_2	x_3	x_4	x_5
1	70400	0.934	78.06	118.03	404.17	1.80	72.25
2	95175	1.269	68.26	125.01	428.21	1.89	64
3	65025	1.897	68.26	125.01	489.08	1.81	64
4	10263	1.130	68.26	125.01	490.76	1.76	72.25
5	25319	1.318	68.26	125.01	569.68	1.78	72.25
6	95190	1.548	68.26	125.01	504.45	1.85	72.25
7	30325	0.762	68.26	125.01	452.58	1.81	72.25
8	80101	1.740	58.45	131.99	621.72	1.95	64
9	80102	1.607	58.45	131.99	509.78	1.71	72.25
10	65022	1.583	58.45	131.99	511.64	1.67	72.25
11	45515	1.487	74.14	149.09	393.77	1.75	72.25

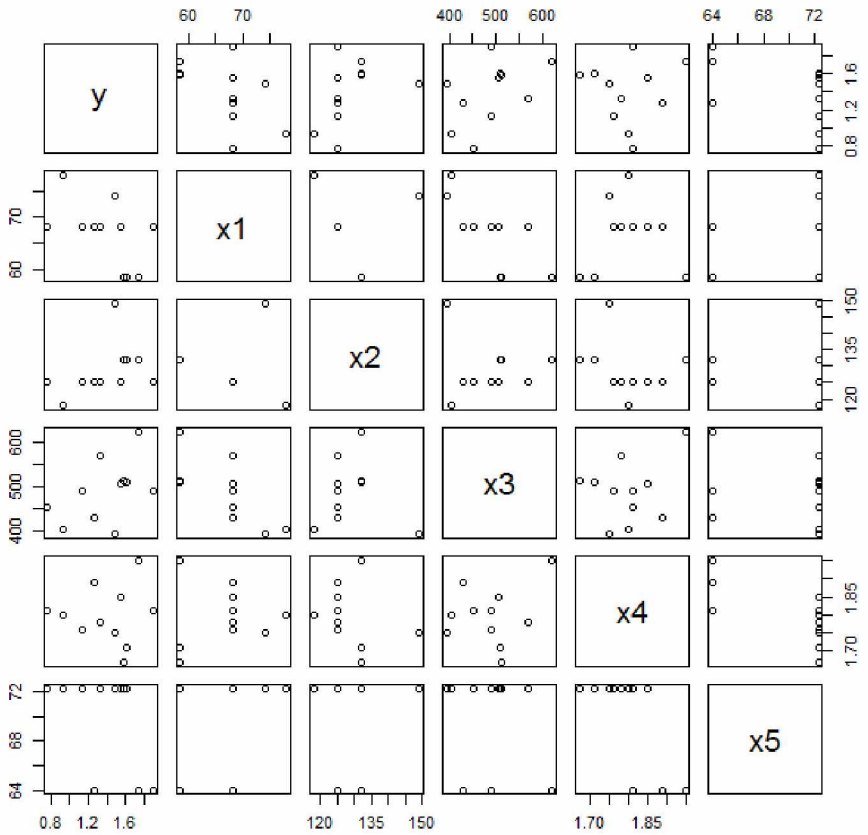

Figure 3.25 Scatter plot matrix for the uniformity index prediction variables

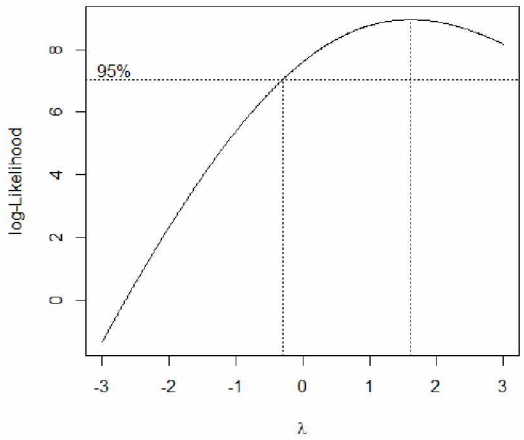

Figure 3.26 Box-Cox result for the uniformity index prediction variables

The Box-Cox normality plot shows that the maximum value of the correlation coefficient is at $\lambda = 1.7$, which is near two. If lambda equals two, in this case the square root transformation appears to be necessary for the model based on the Box-Cox plot.

Based on the Box-Cox transformation and the scatter plot matrix, the response variable was transformed to its square root value. The "energy per unit volume" was transformed to its logarithmic value and the "ratio of bench height to burden" was transformed to its reciprocal value.

	Y	x1	x2	x6	x7	x5
Y	1.00000000	-0.5166012	0.35789972	0.4708133	-0.04133478	-0.49629018
x1	-0.51660118	1.0000000	-0.16651547	-0.7378668	-0.11499035	0.20458665
x2	0.35789972	-0.1665155	1.00000000	-0.1124309	0.27237767	0.09061634
x6	0.47081333	-0.7378668	-0.11243094	1.0000000	-0.18074652	-0.20964107
x7	-0.04133478	-0.1149904	0.27237767	-0.1807465	1.00000000	0.67631607
x5	-0.49629018	0.2045867	0.09061634	-0.2096411	0.67631607	1.00000000

Figure 3.27 Correlation matrix for the uniformity index prediction variables

According to the correlation matrix in Figure 3.27, the uniformity index is strongly related to "Young's modulus" and moderately related to other variables, excluding "Ratio of bench height to burden." "Young's modulus" is strongly related to "energy per volume."

```
Call:
lm(formula = Y ~ x1 + x2 + x3 + x6 + x5 + x1 * x2)

Residuals:
         1          2          3          4          5          6          7          8
-4.184e-18  8.902e-02 -6.889e-02 -4.305e-01 -1.548e-02  4.869e-01 -6.101e-02 -2.013e-02
         9         10         11
 5.640e-02 -3.627e-02  1.291e-17

Coefficients:
             Estimate Std. Error t value Pr(>|t|)
(Intercept) -868.56913  164.81586  -5.270  0.00621 **
x1             3.39485    0.75902   4.473  0.01105 *
x2             1.95822    0.42485   4.609  0.00996 **
x3            -0.22232    0.04282  -5.192  0.00655 **
x6           117.96099   22.26591   5.298  0.00610 **
x5            -0.24135    0.03840  -6.285  0.00327 **
x1:x2         -0.02468    0.00557  -4.431  0.01142 *
---
Signif. codes:  0 '***' 0.001 '**' 0.01 '*' 0.05 '.' 0.1 ' ' 1

Residual standard error: 0.3331 on 4 degrees of freedom
Multiple R-squared:  0.9473,    Adjusted R-squared:  0.8683
F-statistic: 11.98 on 6 and 4 DF,  p-value: 0.01551
```

Figure 3.28 Summary of the model for uniformity index

Model selection criteria were applied to the transformed model and only one model was created. "The ratio of bench height to burden" was eliminated during the model selection step. The model was statistically significant; therefore, the model can be selected.

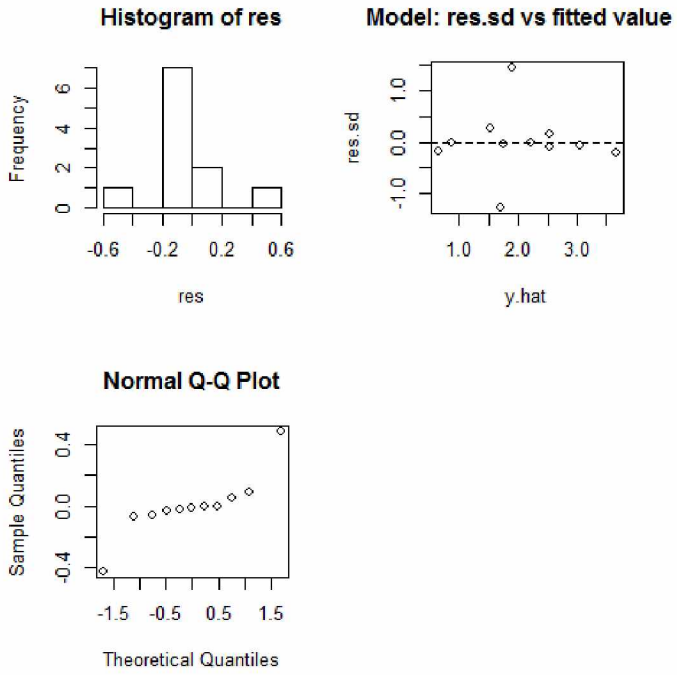

Figure 3.29 Histogram of residual, residual plot, and qq plot of diagnostic for the model of uniformity index

The histogram is not well shaped. On the residual plot, all points are inside of ±1.5 standard deviations. Normal qq plot is skewed because of the outliers. The outliers were checked again, which were patterns of the lowest and highest strength rocks. For the project, all four variance inflation factors for each predictor variable were calculated and the results did not exceed the limitation of 10, indicating that serious multicollinearity problems do not exist.

The model for uniformity index is:

$$n^2 = -868.569 + 3.395E + 1.958\sigma_c - 0.222\left(\frac{En}{V}\right) + 117.961\ln\left(\frac{En}{V}\right) - 0.241(B * S) - 0.025(E * \sigma_c)$$

This model can be expressed as:

$$n = \sqrt{-868.569 + 3.395E + 1.958\sigma_c - 0.222\left(\frac{En}{V}\right) + 117.961\ln\left(\frac{En}{V}\right) - 0.241(B * S) - 0.025(E * \sigma_c)} \qquad (3.2)$$

The uniformity indices, characteristic sizes, and mean sizes for each blasting pattern were predicted, using the newly created regression models and Rosin-Rammler distribution equation. In addition, the fragment size distribution curves were plotted. The results and the rock fragment size distribution are shown in Table 3.14 and Figure 3.30-3.33.

Table 3.14 The results of the regression model

	Pattern number	Uniformity Index, n	Mean Size, P50, (mm)	Characteristic Size, X_C (mm)
1	70400	0.93	225.36	332.66
2	95175	1.23	173.25	231.89
3	65025	1.91	101.81	122.99
4	10263	1.30	83.47	107.99
5	25319	1.32	139.35	182.81
6	95190	1.38	101.58	132.22
7	30325	0.80	74.89	113.56
8	80101	1.74	59.55	70.84
9	80102	1.59	236.57	297.42
10	65022	1.59	190.13	301.83
11	45515	1.48	158.59	202.19
Minimum		0.80	59.55	70.84
Overall Average		1.39	140.41	190.58
Maximum		1.91	236.57	332.66
Standard Deviation		0.33	61.17	89.97

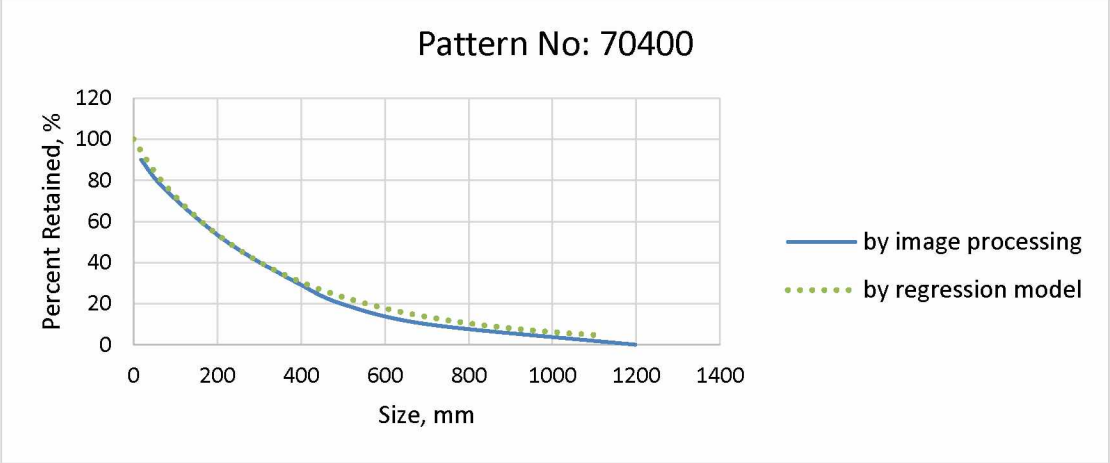

Figure 3.30 A comparison of the rock fragment size distribution between image processing and regression model for hardness factor 12

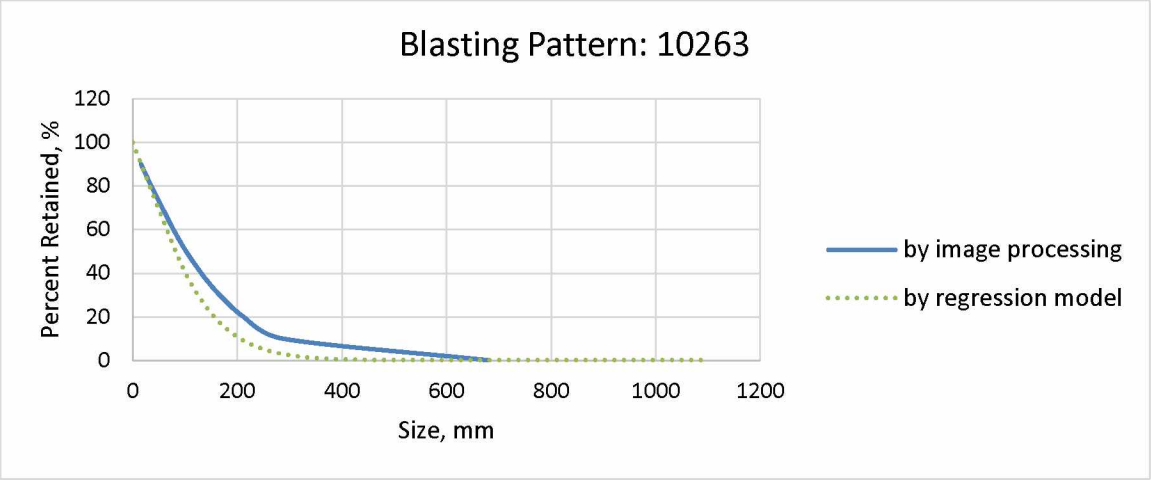

Figure 3.31 A comparison of the rock fragment size distribution between image processing and regression model for hardness factor 13

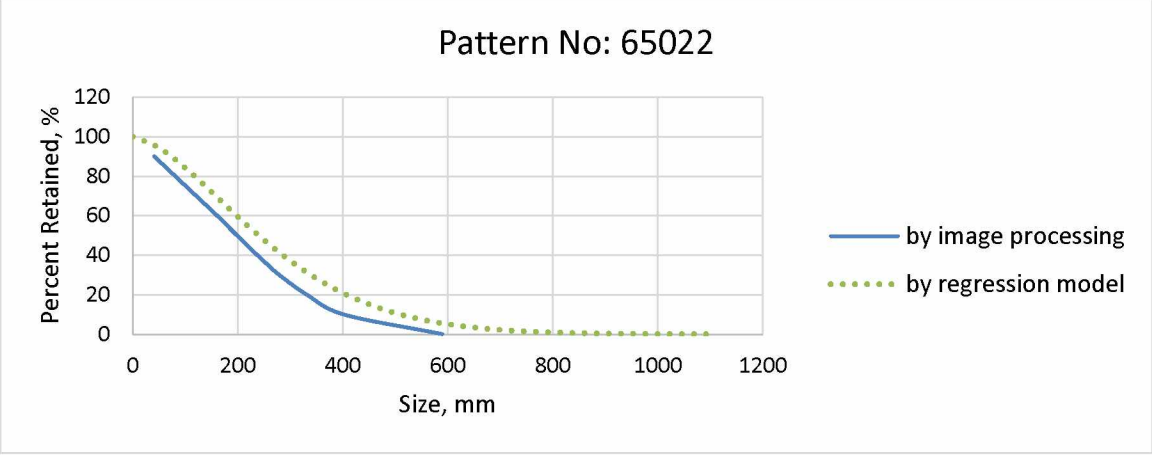

Figure 3.32 A comparison of the rock fragment size distribution between image processing and regression model for hardness factor 14

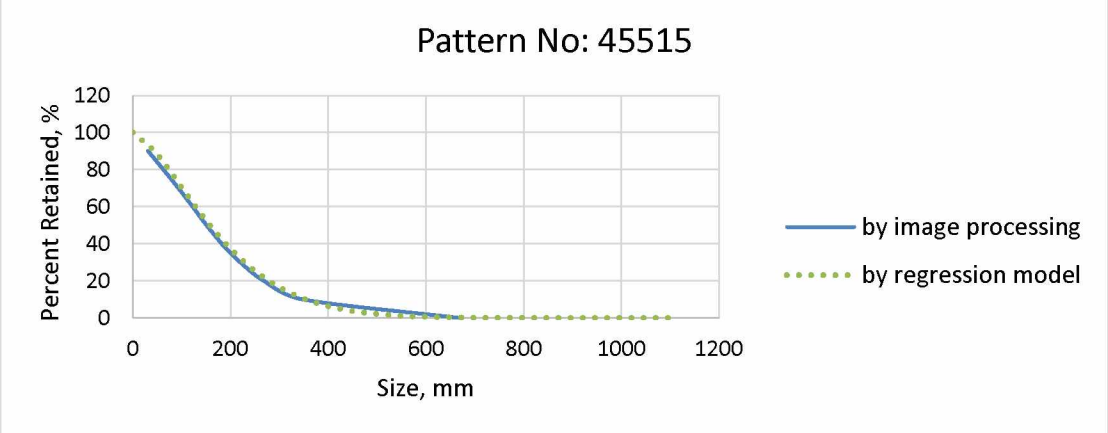

Figure 3.33 A comparison of the rock fragment size distribution between image processing and regression model for hardness factor 15

Table 3.15 Comparison of the uniformity indices and the mean sizes between the image processing and the regression model

Patterns	Hardness Factor	Measured (Image Processing)		Predicted (Regression model)	
		Uniformity Index	Mean Size, mm	Uniformity Index	Mean Size, mm
70400	12	0.93	223.38	0.93	225.36
10263	13	1.13	102.29	1.30	83.47
65022	14	1.58	198.61	1.59	190.13
45515	15	1.49	151.13	1.48	158.59

Figure 3.31-3.34 and Table 3.15 show the comparisons of the rock fragment size distributions of image processing and the regression model for different rock types. The rock types were granite and granodiorite for Pattern70400, granite porphyry and highly fissured granodiorite porphyry for Pattern10263, fine-grained granodiorite for Pattern65022, and trahidacite, trahi-riolit, and trahi-granite for Pattern45515.

The predicted value of Pattern10263 by regression model differs significantly in uniformity and fragment size. Its reason can be related to rock mass structure, which was highly fissured granodiorite porphyry. Most results of the regression model were very similar to the value of the image processing which means the regression model fits well.

3.4.3 Summary of Multivariate Regression Models

The multivariate regression models were developed for the predictions of the fragment characteristic size and the uniformity index. Values of passing percent were estimated for every 50 mm starting from 0 to 1200 mm with regression model. The fragment size distribution curves were plotted (Figure C.1 to C.6).

The regression model indicates that the parameters most related to the fragment characteristic size are the “energy per unit volume” and the “ratio of bench height to burden.”

The parameters most related to the uniformity index were the “Young’s modulus”, “energy per unit volume” and the “area per blasthole.”

Chapter 4 Discussions and Comparisons

The rock fragment size distributions were evaluated using the most popular image processing method, the Kuz-Ram prediction model and the multivariate regression model. The results from these measurements and predictions were compared with each other. Some observations on the digital image measurements and the two prediction models are presented below.

4.1 Discussions

1. Employing the Split-Desktop software, the rock fragment size distributions at the Erdenet Mine were determined for each blasting pattern.

- Image taking orientation is important and the best orientation is the orientation of the scaling objects are perpendicular to the axis of the camera. In the study, the camera aimed from five different positions to the same point. Among the images that were used as the inputs for the image processing program, some were taken from the only perpendicular orientation and some were taken from the mid three positions (the position of the perpendicular orientation and its nearest two side positions).

  Spherical bodies were used as the scaling objects; thereby the skewing was reduced to minimum.
- For obtaining more accurate information, images should be taken from more than one place on the same muckpile. In the study, images were taken from two different places on three blasting patterns and processed.
- The muckpile images can be taken not only from muckpile surface, but also during shovel loading operations. In this way, more complete information on the fragment sizes can be obtained at different layers from the top to the bottom of the muckpile.
- In this study the values of fines cutoff were 41 mm to 137 mm. They were measured automatically based on image resolution or pixel/unit.
- The fines factor influences the size calculations. It can be manually adjusted by the operator. In the study, the results from one of the blasting patterns were investigated with fines factor varied from 10% to 50%. It appeared that the fragment sizes reduced only by 5mm, which was not a significant difference. In the study, the fines factors were determined by observations of the images and were ranged from 20% to 75%.

2. The rock factor is the key parameter for fragment size distribution prediction by the Kuz-Ram model.

- For more reasonable results, the face dip direction, joint plane orientation, joint plane spacing should be clearly identified.
- Kuznetsov (1973) suggested that the rock factor should be 7 for medium rocks to 13 for hard rock. Cunningham (1983) indicated that the rock factors should be ranged from 8 to 12. In the current study, the rock factor varied from 5.92 to 6.28. Most of the Kuz-Ram model predictions and the measured fragment size distribution curves were very different. The fragment size distributions predicted by the Kuz-Ram model were much bigger than the measured values with Split-Desktop software.
- Statistical analyses were performed on the fragment size distributions measured with the digital imaging method against a number of geological and blasting parameters. Multivariate nonlinear regression models were developed for fragment size distribution prediction due to rock blasting at the Erdenet mine site. A total of eleven sets of blasting data were collected and analyzed. Models were statistically significant.
- The uniformity and size distributions were separately measured for four different rock types using the image processing method. In future work, more blasting data should be collected from the mine site, and the regression models can be created for each rock type. However, due to the small number of data sets, the model validation is limited. Therefore, for a more reasonable regression model, we need more data.

4.2 Comparisons of Results

Comparisons among the results of the fragment size distributions by the digital image measurements, the Kuz-Ram model predictions and the multivariate regression model predictions are presented below.

The mean uniformity values of by the digital image measurements, the Kuz-Ram model predictions, and the regression model predictions were 1.39, 1.10, and 1.39, with standard deviations of 0.34, 0.02, and 0.33 respectively.

Based on the standard deviations, the uniformity of the Kuz-Ram model was more uniform, but fragment sizes of the regression model and image processing were non-uniform. The regression model appeared to be more in agreement with the digital image measurements and the Kuz-Ram model showed some discrepancies with the measurements. It also indicated that there is a need for improvement at the Erdenet mine rock blasting for better rock fragment size uniformity.

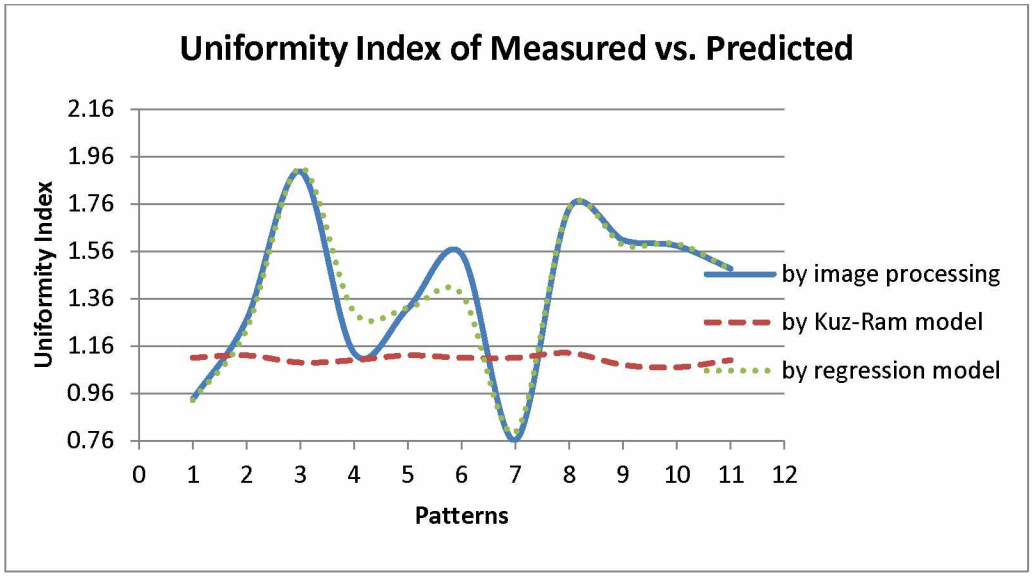

Figure 4.1 Comparison of the fragment size distribution uniformities

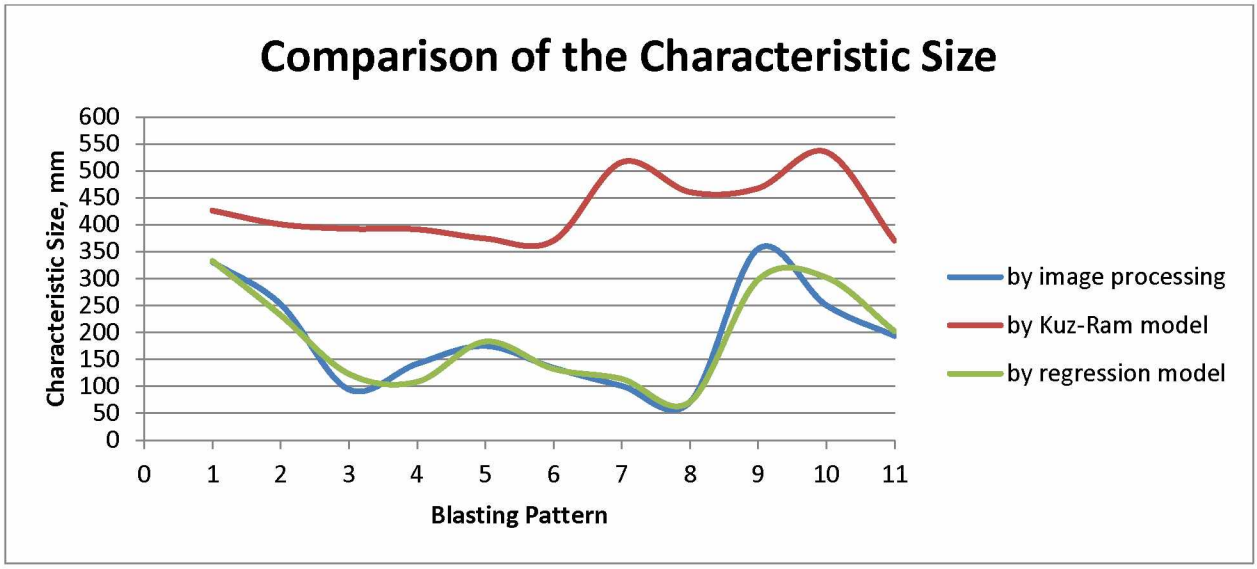

Figure 4.2 Comparison of the characteristic size

The mean fragment characteristic sizes of the image processing measurements, the Kuz-Ram model predictions and the regression model predictions were 190.61mm, 397.53mm and 192.10mm, respectively. The characteristic size (screen size with a passing percentage of 63.2%) of the Kuz-Ram was 108.55 % greater than the image processing measurements, but the

regression model was only 0.78 % greater than the measurements, indicating a significant improvement of the regression model over the Kuz-Ram model. However, the limitation for the regression model is that it is site-specific for the Erdenet mine. Although the regression model developed in this study may not be applicable to other mine sites with different geological and blasting conditions, the approach applied in the development of the multivariate nonlinear regression models in this study may well be applied in other mine blasting settings.

Chapter 5 Conclusion and Future Work

In this project, blasting performances for eleven different blasting patterns at the Erdenet mine were evaluated. The rock fragment size distributions were measured using the digital image processing method. With some limitations, the Split-Desktop program appeared effective. A better and more objective method for the determination of the fines cutoff size is desirable to improve the accuracy and efficiency of the image processing measurements of the rock fragment size distributions. The Kuz-Ram model is the most well-known prediction model for rock fragment size distributions. The predictions by the Kuz-Ram model required a key parameter of the Rock Factor. There appeared to be some discrepancy between the current study and studies by other researchers on the value range of this Rock Factor. Further studies will be needed in this area. Based on the fragment size distributions measured by the digital image processing method and the associated geological and blasting parameters, including the rock properties, the explosive properties, and the blasting design parameters, statistical analyses were performed and multivariate nonlinear regression models were developed for the predictions of the fragment characteristic size and the uniformity index. The models are statistically significant and provide close predictions of these key fragment size distribution parameters. However, the validation of the models is limited due to the small size of the sample data.

When comparing the image processing measurements with the predicted results by the Kuz-Ram model, the fragment sizes by the Kuz-Ram model predictions were approximately two times larger than the image processing measurements. Among different blasting patterns, the fragment size distribution curves predicted by the Kuz-Ram model were much smoother (more uniform) than that of the image processing measurements, indicating a significant discrepancy between the Kuz-Ram model predictions and the measurements. It may imply that more accurate input parameters for the Kuz-Ram model are needed for a better prediction and further improvement of the Kuz-Ram model may also be desirable.

The multivariate nonlinear regression models developed in this study provide another mean for the predictions of rock fragment size distributions at the Erdenet mine. The regression models for the determinations of the uniformity index and the characteristic size were statistically significant. The rock fragment size distributions predicted by the regression models showed close agreement with the digital image processing measurements. The models appeared to be

effective tools for the fragment size prediction at the mine. In future work, more data should be collected for further improvement and validation of the regression models.

The rock mass RMR (Rock Mass Rating) values can be a significant variable for the multivariate regression analysis. It combines the most significant geologic parameters defining the rock mass properties with one overall comprehensive index of rock mass quality. It could be a very effective predictor for the regression model.

Based on the digital image processing measurements and the regression analyses, the blasting fragment size distributions at the mine site appeared to be non-uniform and significant variations in fragment size distributions existed among different blasting patterns, which would cause inefficiency at the milling plant. It is advisable that measures be taken to improve the uniformity of fragment sizes throughout various blasting sites at the mine.

References

Ashitosh, Devgan. Analysis of rock fragmentation using digital image processing. Thesis.University of Arizon, 1992

Ashitosh D, Kemeny, John M., et al. "Analysis of rock fragmentation using digital image processing." Journal of Geotechnical Engineering 119.7 (1993): 1144-1160.

Cunningham, CVB. "The Kuz-Ram Model for Prediction of Fragmentation from Blasting." First International Symposium on Rock Fragmentation by Blasting (1983): 439-54. Web.

Cunningham, CVB. "Fragmentation Estimations and the Kuz-Ram Model." Second International Symposium on Rock Fragmentation by Blasting (1987): 475-87. Web.

Esen, S., H. A. Bilgin, and T. BoBo. "Effect of explosive on fragmentation." The 4th Drilling and Blasting Symposium, Ankara, Turkey. 2000.

Explosives and Rock Blasting. Dallas: Atlas Powder, 1987. Print.

Gerel, O., and B. Munkhtsengel. "Erdenetiin Ovoo Porphyry Copper–molybdenum Deposit in Northern Mongolia." Porter, T.M. (Ed.), Super Porphyry Copper and Gold Deposits: A Global Perspective. Vol. 2. Adelaide: PGC, 2005. 525-43. Print.

Havermann, T., and W. Vogt. "TUCIPS-A system for estimation of fragmentation after production blasts." J.A. Franklin & T.Katsabanis (eds.), Measurement of Blast Fragmentation. Rotterdam: Balkema, 1996. 67-72.

Heiniö, Matti. Rock Excavation Handbook. N.p.: Sandvik Tamrock, 1999. Print.

Hustrulid, William. Blasting Principles for Open Pit Mining. Vol. 1. Rotterdam: Balkema, 1999. Print.

ISEE. Blasters' Handbook. 18th ed. Cleveland, OH: ISEE, 2011. Print.

Kanchibotla, Sarma S., Walter Valery, and Steve Morrell. "Modelling fines in blast fragmentation and its impact on crushing and grinding." Explo '99–A conference on rock breaking, The Australasian Institute of Mining and Metallurgy, Kalgoorlie, Australia. 1999.

Kutner, Michael H., Christopher J. Nachtsheim, and John Neter. Applied Linear Regression Models / Michael H. Kutner, Christopher J. Nachtsheim, John Neter. Boston, MA: McGraw-Hill/Irwin, 2004. Print.

Kuznetsov, VM. "The Mean Diameter of Fragments Formed by Blasting Rock." Soviet Mining Science (1973): 144-48.

Laikhansuren, B. Blasting Technology and Optimization of Blast Design Parameters. Ulaanbaatar: MUST, 2000. Print.

Lilly, PA. An Empirical Method of Assessing Rock Mass Blastability. Newman: Large Open Pit Mining Conference, 1986. Print.

Lilly, PA. "The Use of Blastability Index in the Design of Blasts for Open Pit Mines." Proceedings of the Western Australian Conference on Mining Geomechanics (1992): 421.

Maerz, Norbert H., Tom C. Palangio, and John A. Franklin. "WipFrag image based granulometry system." Proceedings of the FRAGBLAST 5 Workshop on Measurement of Blast Fragmentation, Montreal, Quebec, Canada. AA Balkema, 1996.

Malyutin, Yu. A., I. E. Maksimyuk, S. P. Gavrilova, A. L. Zhigachev, and P. Erdenetsogt. "Geological and Geochemical Features of the Erdenetiin-Ovoo Deposit." Moscow University Geology Bulletin 62.5 (2007): 325-33. Web.

Mkwelo, Simphiwe. A machine vision-based approach to measuring the size distribution of rocks on a conveyor belt. Diss. University of Cape Town, 2004.

Nokleberg, WJ, ed. "Late Carboniferous through Early Jurassic Metallogenesis and Tectonics of Northeast Asia, Chapter 7 in Metallogenesis and Tectonics of Northeast Asia." Professional Paper. Reston: U.S. Geological Survey, 2010. 7-26--28. 1765-7. Web.

Nyamdorj, D. Rock Mass and Study of Drilling and Blasting. Ulaanbaatar: Arvin Press, 2009. Print.

Olofsson, Stig O. Applied Explosives Technology for Construction and Mining. Arla, Sweden: APPLEX, 1990. Print.

Prasad, Umesh. "Energy Utilization in Comminution and Its Application to Rock Blasting." (1994).

Sameti, B., and I. Bell. "A Portable Device for Mine Face Rock Fragmentation Analysis." Mining Engineering Magazine Jan. 2015: 16-23.

SPLIT Engineering LLC, Split-Desktop Software Manual, 2011

Venkatesh, M. Limestone Rock Fragmentation analysis Using WipFrag. Diss. National Institute of Technology Rourkela, 2010.

Bobo, Tom, Brian Norton, Kirstin Girdner, and John Kemeny. "Quantifying Your Blast Fragmentation Using Split-Desktop." BAI 2000 High-Tech Seminar. N.p.: ISEE, 2003. Print.

APPENDIX A

Table A.1 Rock types of blasting pattern

Blasting Pattern	Rock types
70400	Granite and granodiorite
95175	Fine-grained, biotite granodiorite
65025	Fine-grained granodiorite
10263	Granodiorite porphyry with fractures
25319	Granodiorite porphyry with fractures
95190	Granite porphyry, and granodiorite porphyry with differently oriented fractures . Dykes with fractures containing syenite-diorite, diorite and basaltic.
30325	Granodiorite
80101	Granite, granodiorite
80102	Granite, granodiorite
65022	Fine-grained granodiorite
45515	Trachydacite, trahi-riolit, trahi-granite

Table A.2 Protodyakonov's hardness factor

Protodyakonov classification of rock hardness.

Category	*Hardness Level*	*Description of Rock*	*Rock Hardness f*
I	Highest	The hardest, toughest and most dense quartzites and basalts.	20
II	Very hard	Very hard granitic rocks, quartz porphyry, siliceous schist, weaker quartzites. Hardest sandstone and limestone.	15
III	Hard	Granite (dense) and granitic rocks. Very hard sandstones and limestones. Quartz veins. Hard conglomerate. Very hard iron ore.	10
IIIa	Hard	Limestones (hard). Weaker granites. Hard sandstones, marble, dolomites and pyrites.	8
IV	Rather hard	Ordinary sandstone. Iron ore.	6
IVa	Rather hard	Sandy schists. Schistose sandstones.	5
V	Moderate	Hard shale. Non-hard sandstones and limestones. Soft conglomerates.	4
Va	Moderate	Various schists (non-hard). Dense marl.	3
VI	Rather soft	Soft schists. Very soft limestones, chalk, rock-salt, gypsum. Frozen soil, anthracite. Ordinary marl. Weathered sandstones, cemented shingle and gravel, rocky soil.	2
VIa	Rather soft	Detritus soil. Weathered schists, compressed shingle and detritus, hard bituminous coal, hardened clay.	1.5
VII	Soft	Clay (dense). Soft bituminous coal, hard alluvium, clayey soil.	1.0
VIIa	Soft	Soft sandy clay, loess, gravel.	0.8
VIII	Earthy	Vegetable earth, peat, soft loam, damp sand.	0.6
IX	Dry Substances	Sand, talus, soft gravel, piled up earth, substances extracted coal.	0.5
X	Flowing	Shifting sands, swampy soil, rare-fractioned loess and other rare-fractioned soils.	0.3

Table A.3 Results of measured by the Split-Desktop, and predicted by the Kuz-Ram model and regression model

		Measured					Predicted					Model				
	Pattern number	n	$\bar{X}$, mm	X_C, mm	Passing % at 400mm	Passing % at 600mm	n	$\bar{X}$, mm	X_C, mm	Passing % at 400mm	Passing % at 600mm	n	$\bar{X}$, mm	X_C, mm	Passing % at 400mm	Passing % at 600mm
1	70400	0.93	223.38	330.84	70.17	85.00	1.11	305.16	426.01	60.67	76.71	0.93	225.36	332.66	69.49	82.30
2	95175	1.27	188.92	252.25	84.31	98.71	1.12	287.56	400.63	63.15	79.05	1.23	173.25	231.89	85.85	96.00
3	65025	1.90	77.47	93.99	100.00	100.00	1.09	279.66	392.33	63.98	79.49	1.91	101.81	122.99	99.99	100.00
4	10263	1.13	102.29	141.49	96.36	97.91	1.10	279.34	391.25	64.10	79.66	1.30	83.47	107.99	99.59	99.99
5	25319	1.32	132.24	174.65	94.58	98.54	1.12	268.62	374.24	65.92	81.46	1.32	139.35	182.81	93.99	99.18
6	95190	1.55	105.84	134.13	98.62	99.95	1.11	264.95	370.21	66.33	81.69	1.38	101.58	132.22	98.99	99.97
7	30325	0.76	62.11	100.47	99.48	100.00	1.11	369.91	515.87	53.02	69.31	0.80	74.89	113.56	93.43	97.67
8	80101	1.74	56.93	70.29	100.00	100.00	1.13	332.27	460.53	57.41	73.98	1.74	59.55	70.84	100.00	100.00
9	80102	1.61	282.46	354.85	70.38	94.31	1.08	331.76	467.43	57.11	72.91	1.59	236.57	297.42	79.81	95.24
10	65022	1.58	198.61	250.39	88.61	100.00	1.07	378.14	534.83	52.07	67.68	1.59	190.13	301.83	79.10	94.94
11	45515	1.49	151.13	193.41	93.20	97.87	1.10	264.16	370.41	66.28	81.50	1.48	158.59	202.19	93.62	99.34
Minimum		0.76	56.93	70.29	70.17	85.00	1.07	264.16	370.21	52.07	67.68	0.80	59.55	70.84	69.49	82.30
Mean		1.39	143.76	190.61	90.52	97.48	1.10	305.60	427.61	60.91	76.68	1.39	140.41	190.58	90.35	96.78
Maximum		1.90	282.46	354.85	100.00	100.00	1.13	378.14	534.83	66.33	81.69	1.91	236.57	332.66	100.00	100.00
Standard Deviation		0.34	72.51	95.82	11.16	4.47	0.02	41.50	58.88	5.24	5.01	0.33	61.17	89.97	10.36	5.20

APPENDIX B

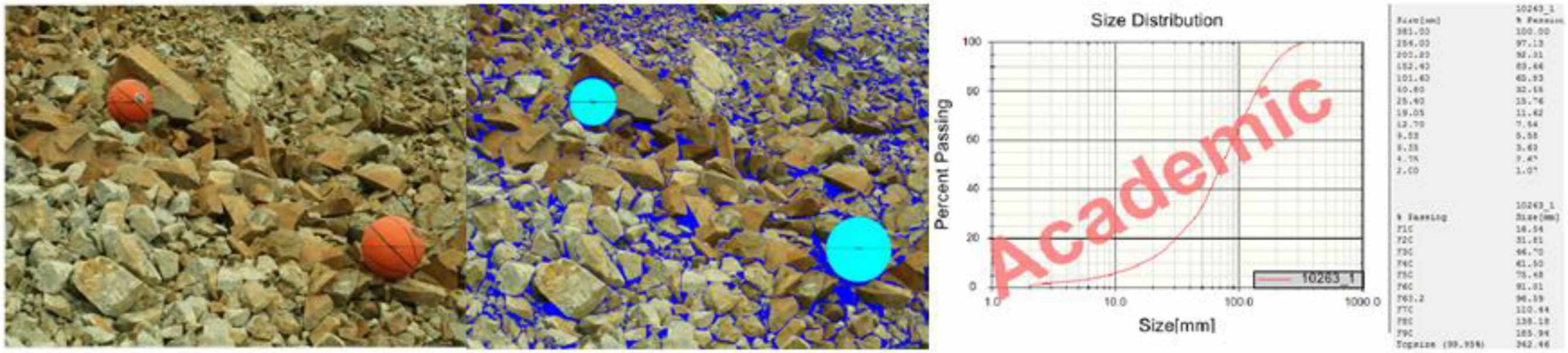

a b c

Figure B.1 Blast pattern of 10263_1: a) the muckpile image, b) the delineated image, c) the size distribution and result of the muckpile

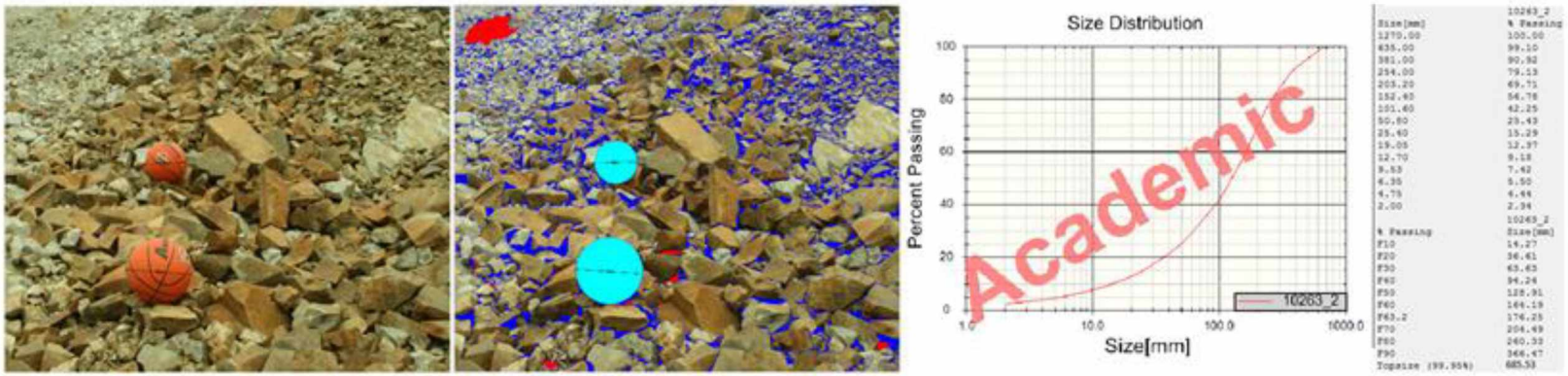

a b c

Figure B.2 Blast pattern of 10263_2: a) the muckpile image, b) the delineated image, c) the size distribution and result of the muckpile

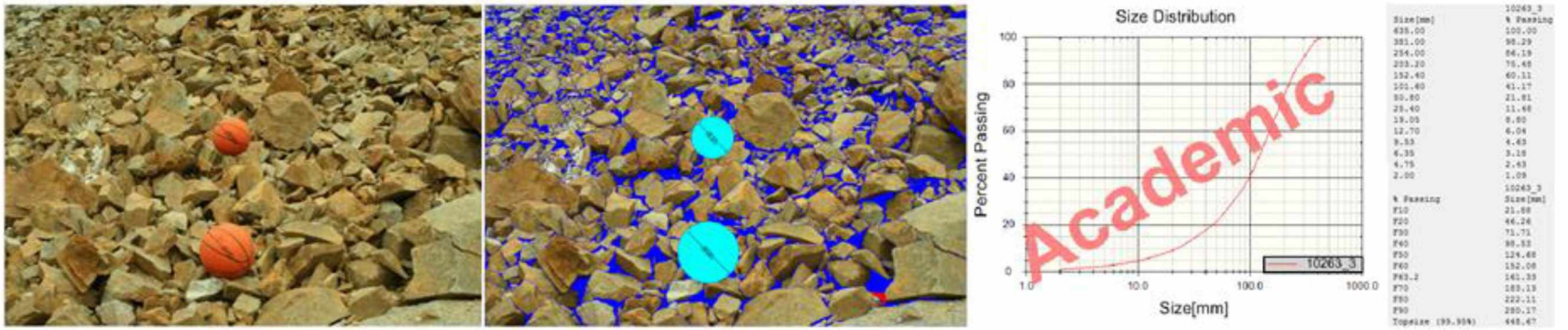

a b c

Figure B.3 Blast pattern of 10263_3: a) the muckpile image, b) the delineated image, c) the size distribution and result of the muckpile

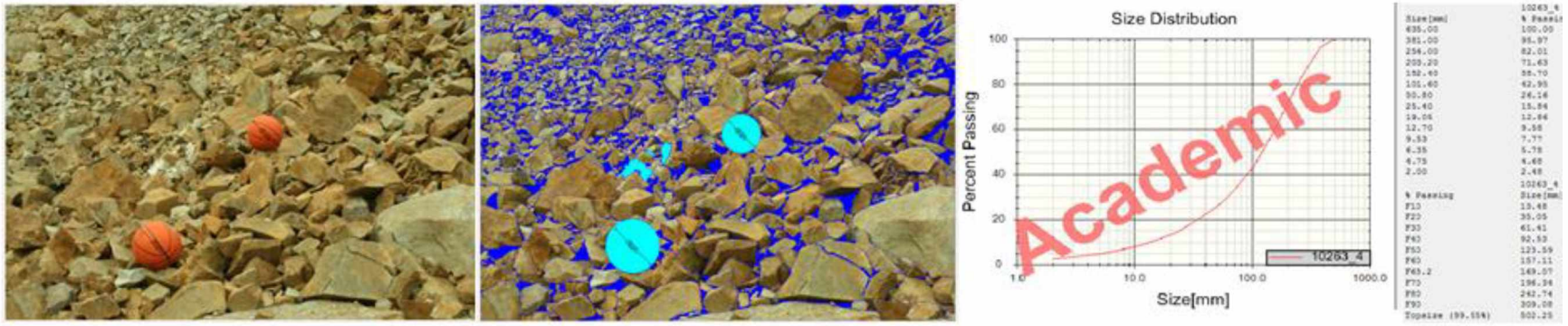

a b c

Figure B.4 Blast pattern of 10263_4: a) the muckpile image, b) the delineated image, c) the size distribution and result of the muckpile

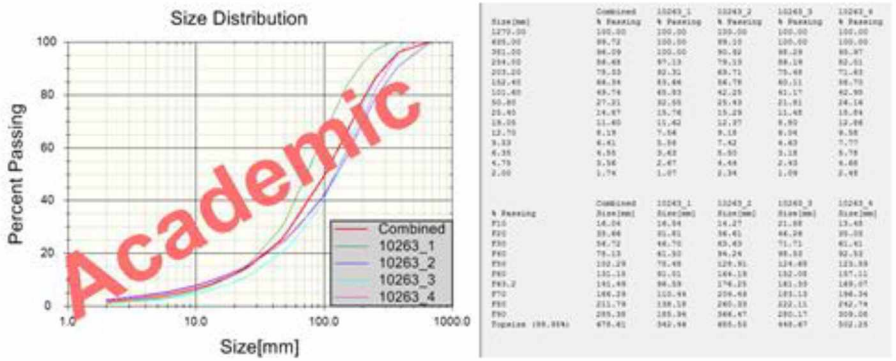

Figure B.5 The combined size distribution and results of blasting pattern of 10263

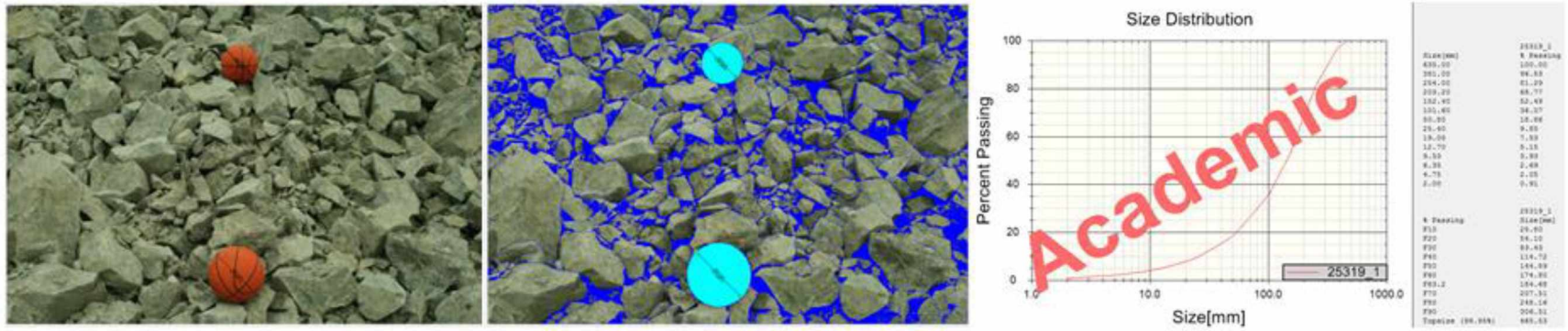

a b c

Figure B.6 Blast pattern of 25319_1: a) the muckpile image, b) the delineated image, c) the size distribution and result of the muckpile

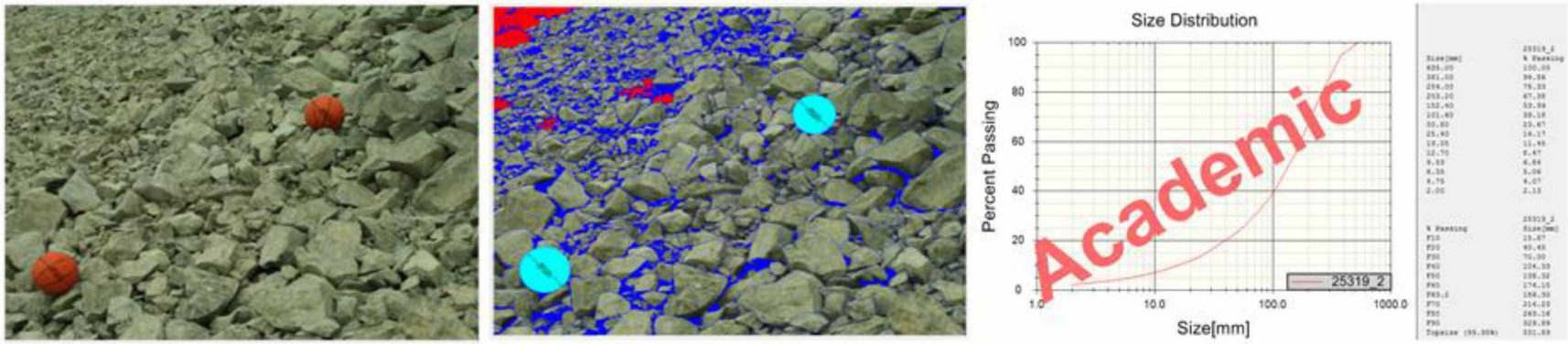

a b c

Figure B.7 Blast pattern of 25319_2: a) the muckpile image, b) the delineated image, c) the size distribution and result of the muckpile

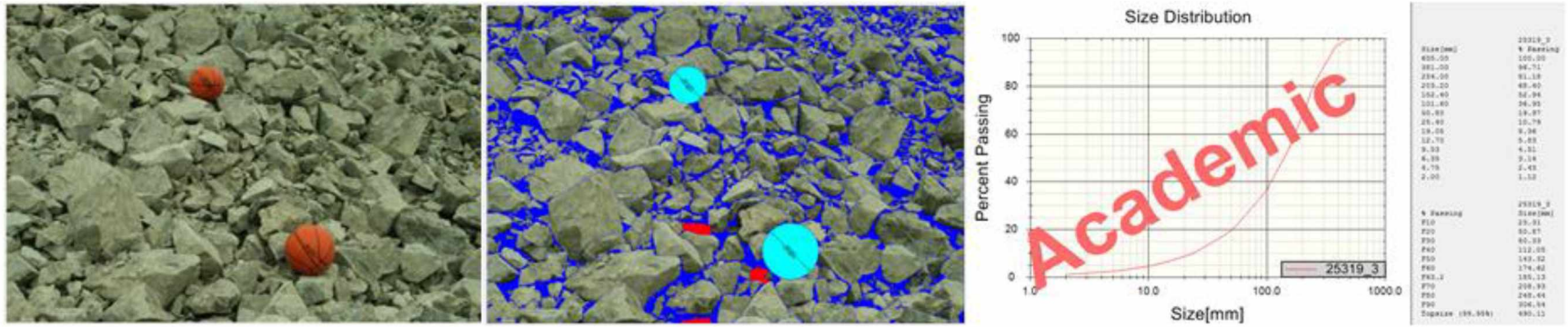

a b c

Figure B.8 Blast pattern of 25319_3: a) the muckpile image, b) the delineated image, c) the size distribution and result of the muckpile

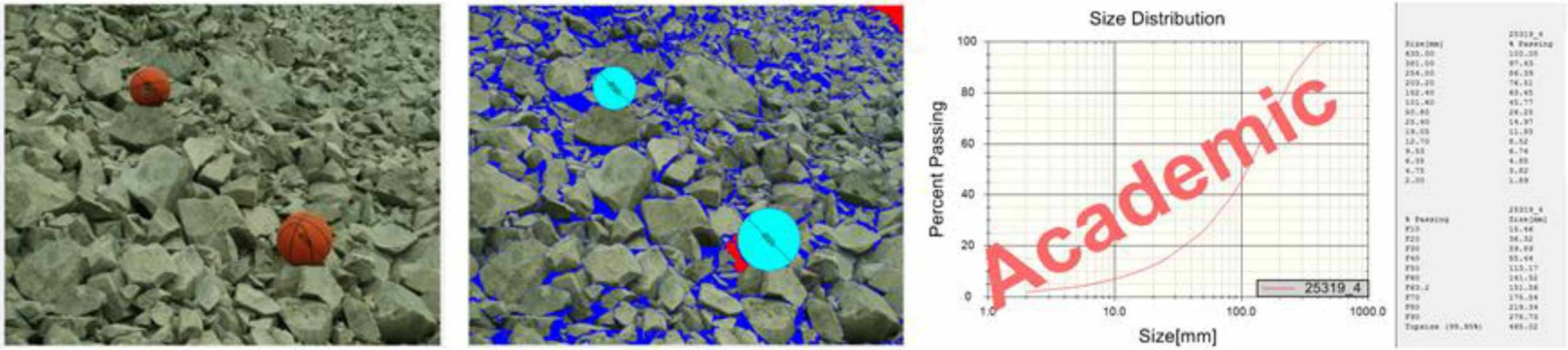

a b c

Figure B.9 Blast pattern of 25319_4: a) the muckpile image, b) the delineated image, c) the size distribution and result of the muckpile

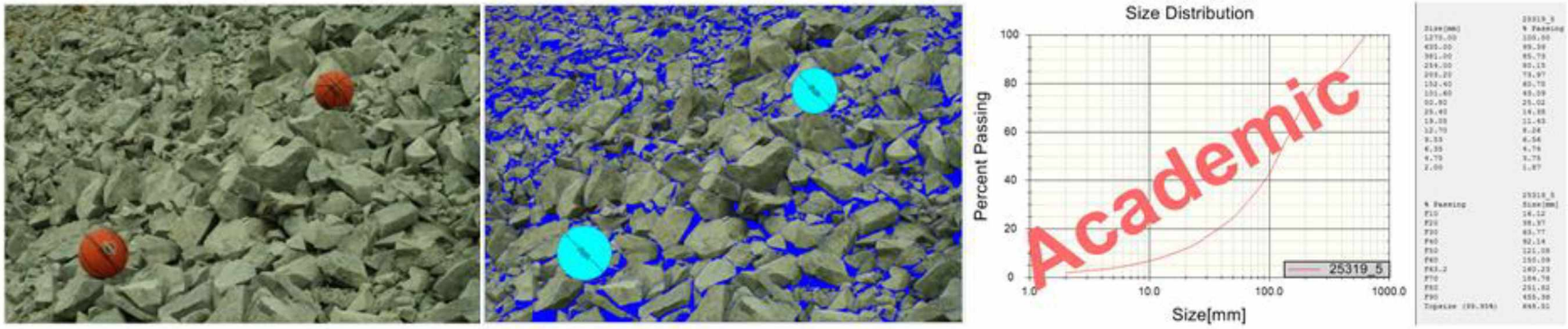

a b c

Figure B.10 Blast pattern of 25319_5: a) the muckpile image, b) the delineated image, c) the size distribution and result of the muckpile

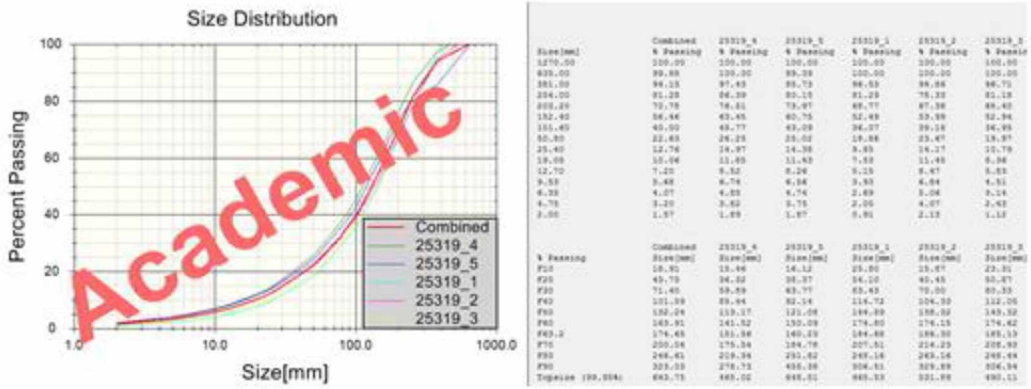

Figure B.11 The combined size distribution and results of blasting pattern of 25319

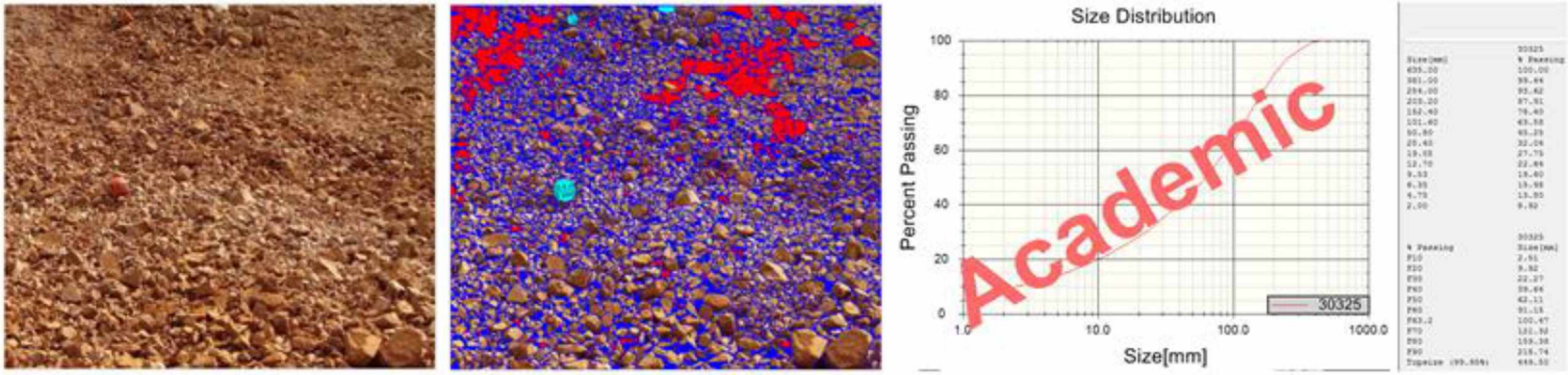

a b c

Figure B.12 Blast pattern of 30325: a) the muckpile image, b) the delineated image, c) the size distribution and result of the muckpile

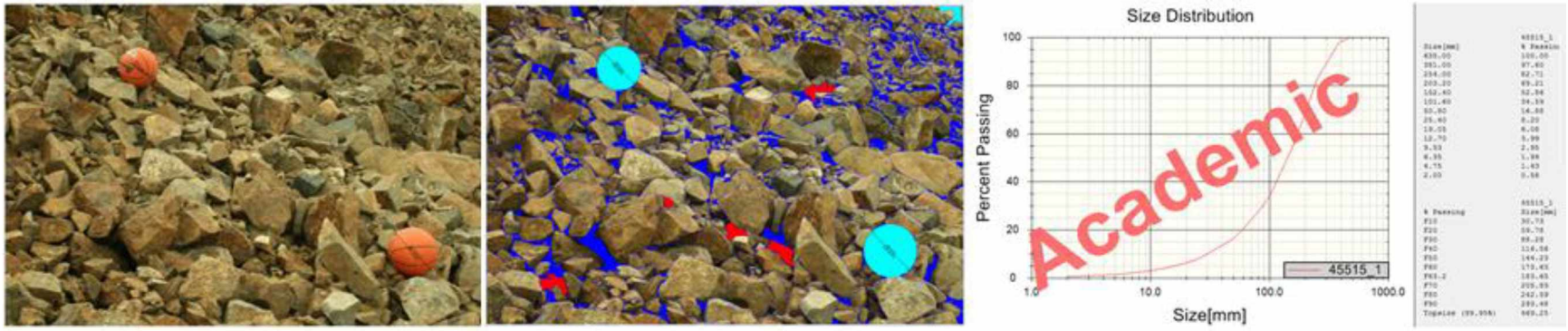

a b c

Figure B.13 Blast pattern of 45515_1: a) the muckpile image, b) the delineated image, c) the size distribution and result of the muckpile

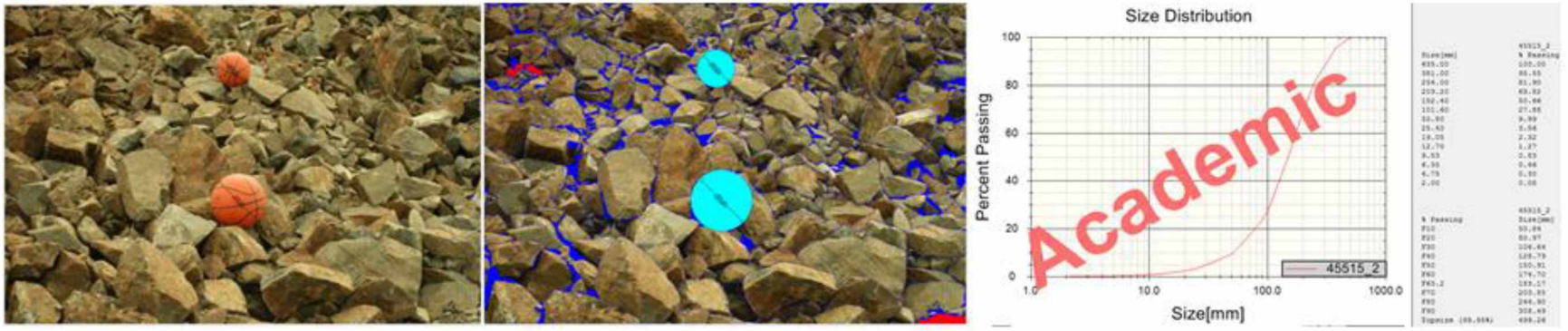

a b c

Figure B.14 Blast pattern of 45515_2: a) the muckpile image, b) the delineated image, c) the size distribution and result of the muckpile

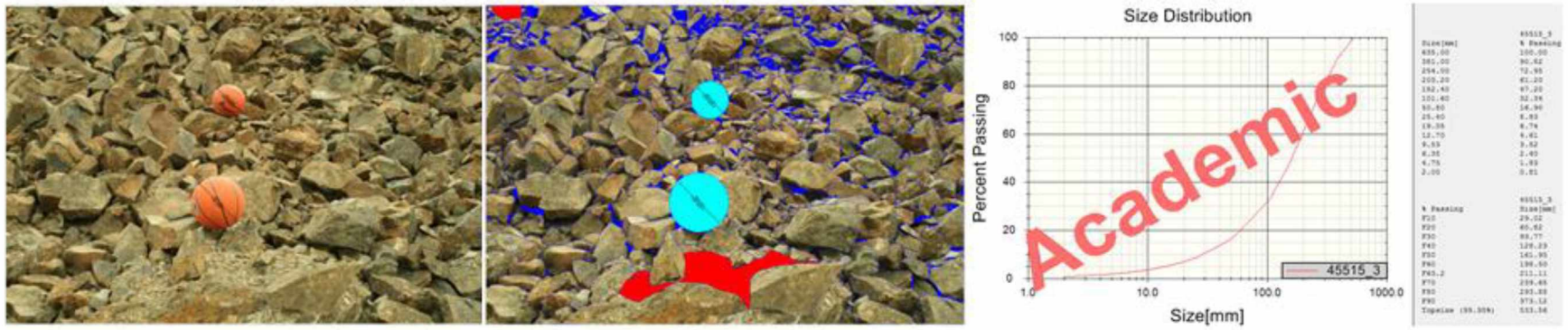

a b c

Figure B.15 Blast pattern of 45515_3: a) the muckpile image, b) the delineated image, c) the size distribution and result of the muckpile

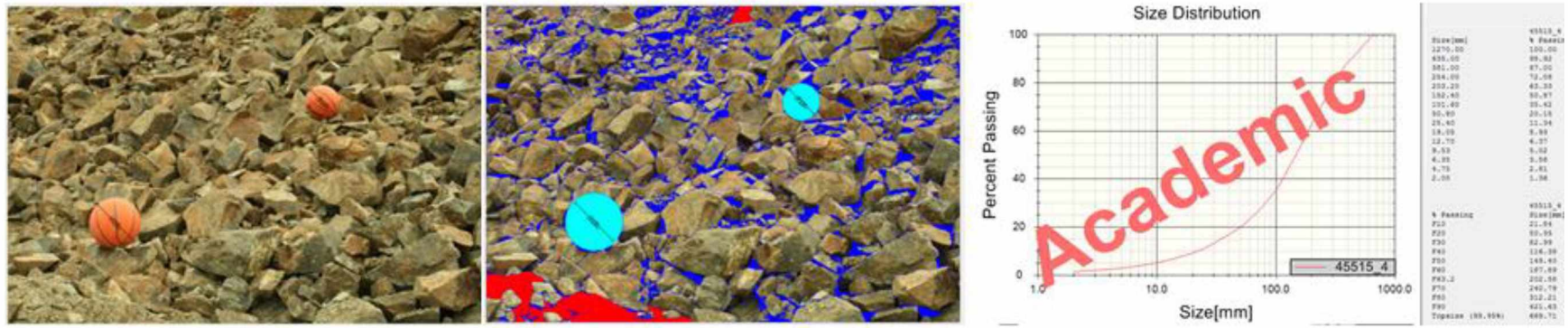

a b c

Figure B.16 Blast pattern of 45515_4: a) the muckpile image, b) the delineated image, c) the size distribution and result of the muckpile

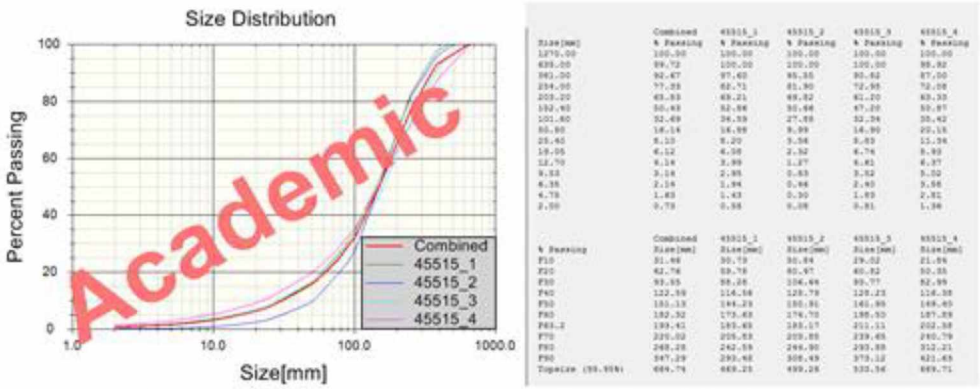

Figure B.17 The combined size distribution and results of blasting pattern of 45515

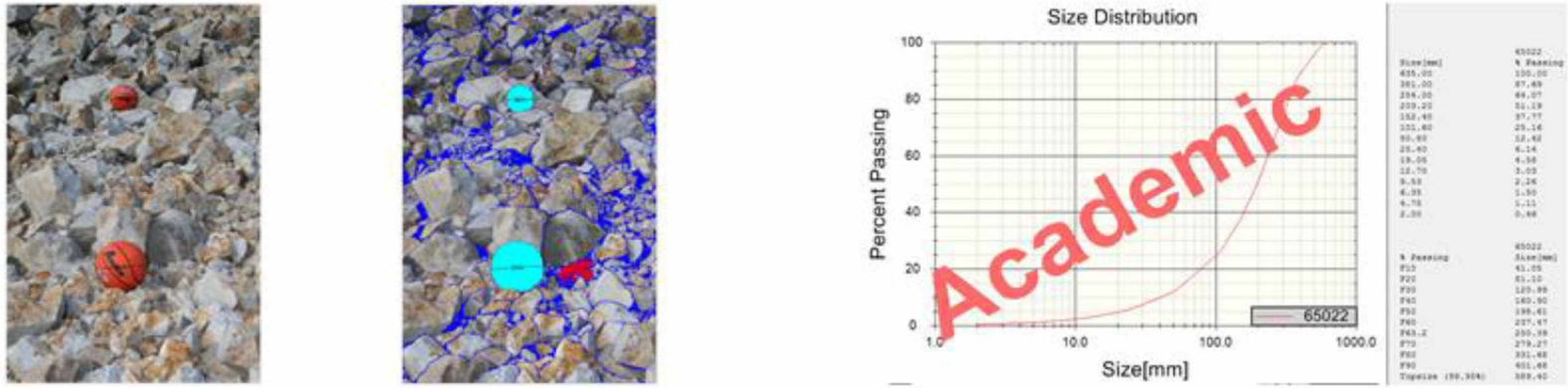

a b c

Figure B.18 Blast pattern of 65022: a) the muckpile image, b) the delineated image, c) the size distribution and result of the muckpile

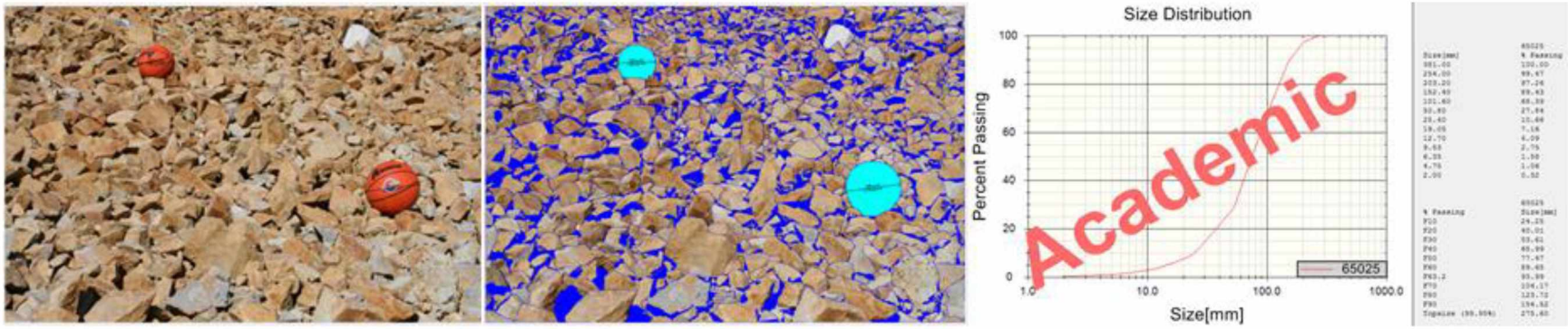

a b c

Figure B.19 Blast pattern of 65025: a) the muckpile image, b) the delineated image, c) the size distribution and result of the muckpile

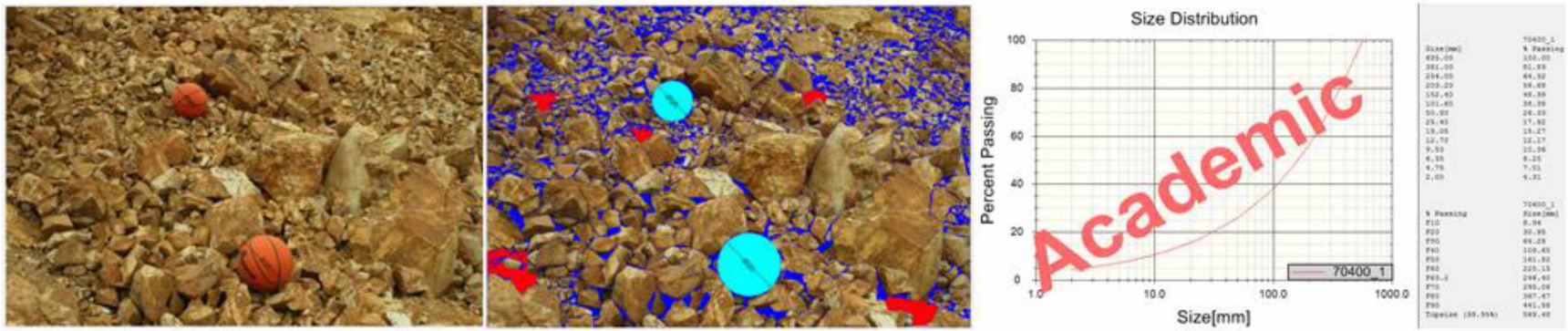

a b c

Figure B.20 Blast pattern of 70400_1: a) the muckpile image, b) the delineated image, c) the size distribution and result of the muckpile

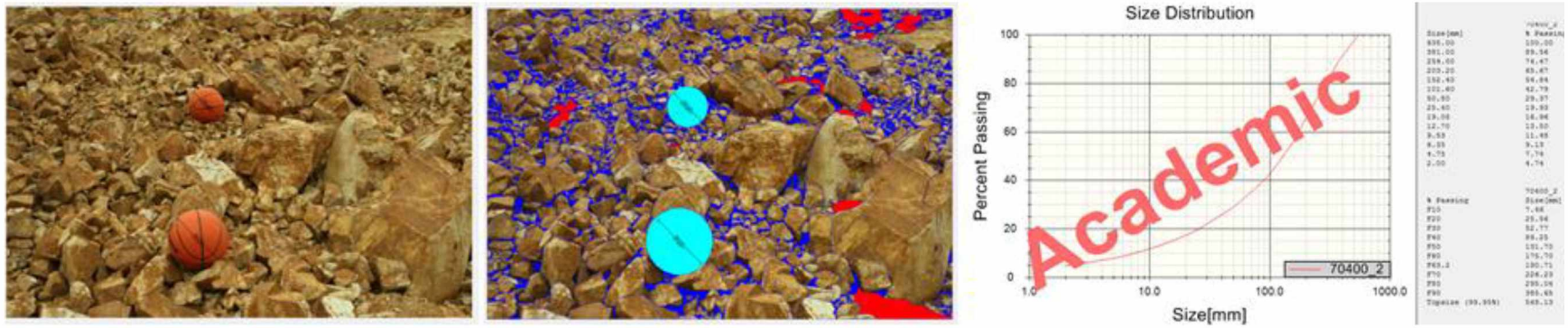

a b c

Figure B.21 Blast pattern of 70400_2: a) the muckpile image, b) the delineated image, c) the size distribution and result of the muckpile

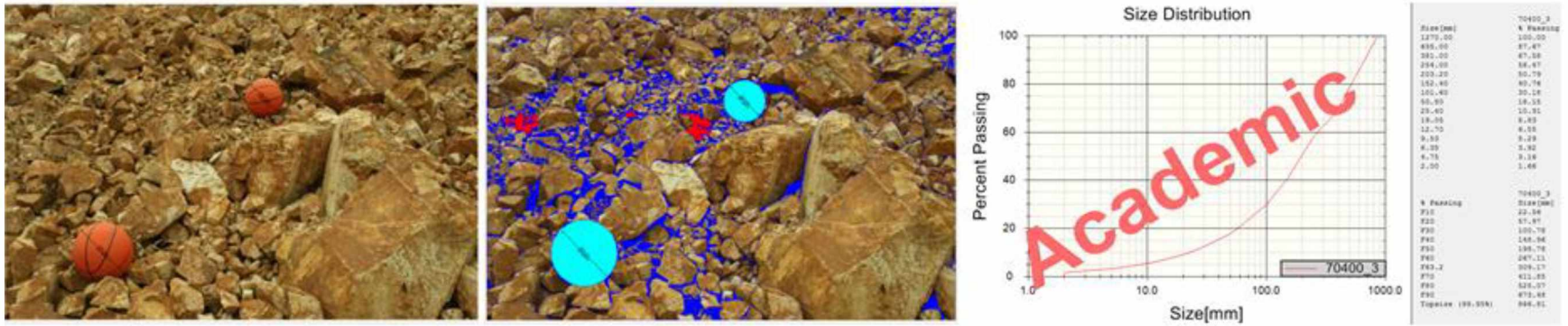

a b c

Figure B.22 Blast pattern of 70400_3: a) the muckpile image, b) the delineated image, c) the size distribution and result of the muckpile

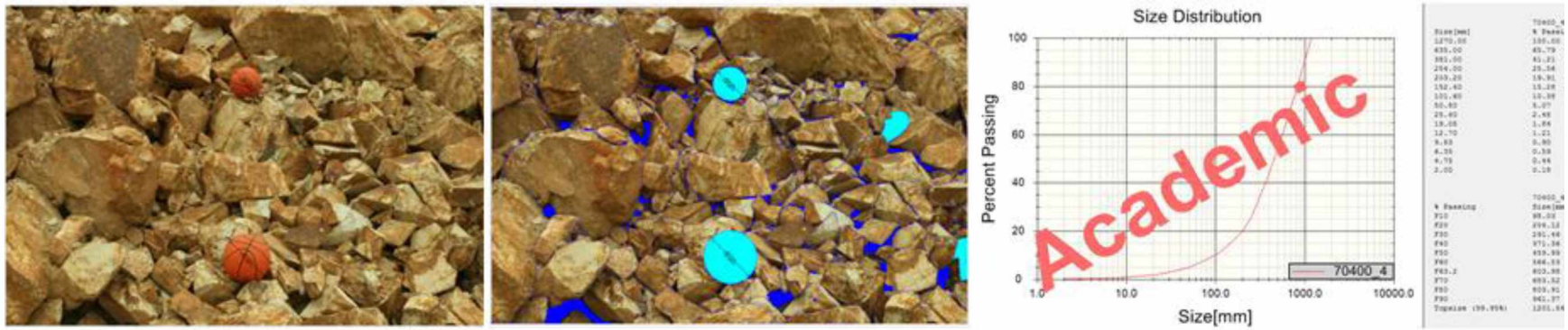

a b c

Figure B.23 Blast pattern of 70400_4: a) the muckpile image, b) the delineated image, c) the size distribution and result of the muckpile

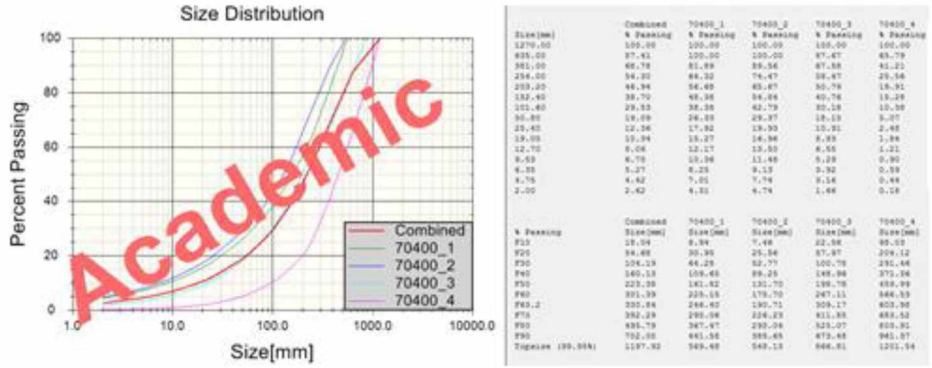

Figure B.24 The combined size distribution and results of blasting pattern of 70400

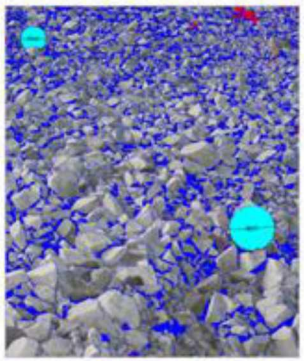

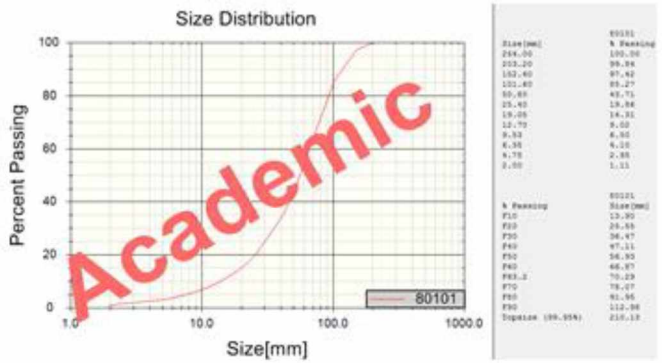

a b c

Figure B.25 Blast pattern of 80101: a) the muckpile image, b) the delineated image, c) the size distribution and result of the muckpile

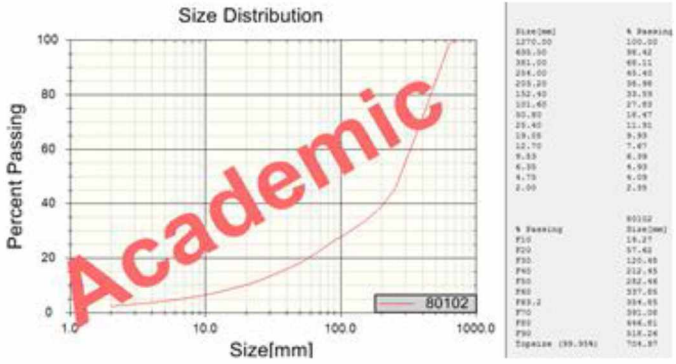

a b c

Figure B.26Blast pattern of 80102: a) the muckpile image, b) the delineated image, c) the size distribution and result of the muckpile

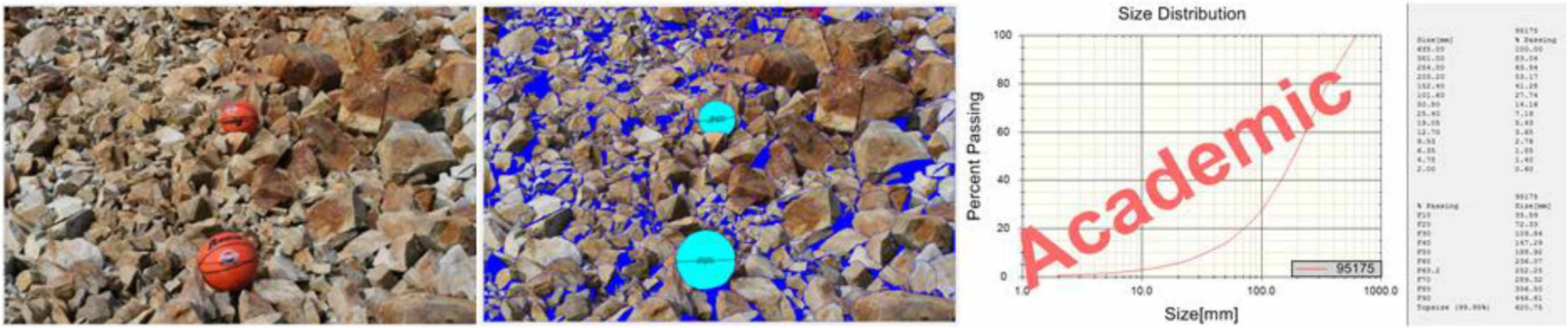

a b c

Figure B.27 Blast pattern of 95175: a) the muckpile image, b) the delineated image, c) the size distribution and result of the muckpile

a b c

Figure B.28 Blast pattern of 95190_1: a) the muckpile image, b) the delineated image, c) the size distribution and result of the muckpile

a b c

Figure B.29 Blast pattern of 95190_2: a) the muckpile image, b) the delineated image, c) the size distribution and result of the muckpile

a b c

Figure B.30 Blast pattern of 95190_3: a) the muckpile image, b) the delineated image, c) the size distribution and result of the muckpile

a b c

Figure B.31 Blast pattern of 95190_4: a) the muckpile image, b) the delineated image, c) the size distribution and result of the muckpile

a b c

Figure B.32 Blast pattern of 95190_5: a) the muckpile image, b) the delineated image, c) the size distribution and result of the muckpile

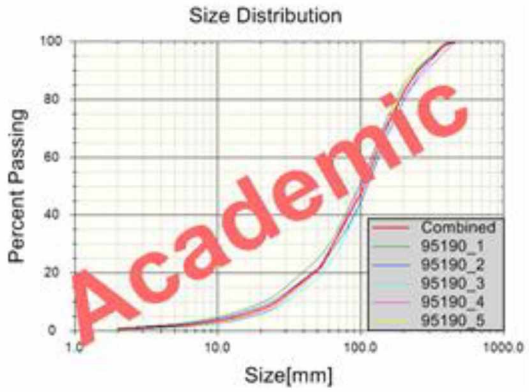

Size[mm]	Combined % Passing	95190_1 % Passing	95190_2 % Passing	95190_3 % Passing	95190_4 % Passing	95190_5 % Passing
635.00	100.00	100.00	100.00	100.00	100.00	100.00
381.00	96.51	98.98	98.41	99.05	96.09	100.00
254.00	89.99	90.96	88.07	90.41	86.83	94.96
203.20	82.89	85.45	80.13	82.49	81.96	89.84
152.40	69.99	79.26	66.66	69.48	71.49	70.04
101.60	47.91	51.38	45.07	44.78	50.38	47.41
50.80	21.57	25.12	21.92	19.48	20.78	20.73
25.40	9.78	12.24	10.46	7.73	8.43	8.94
19.05	7.04	9.11	7.91	5.43	5.62	6.31
12.70	4.45	5.99	5.19	3.24	3.45	3.86
9.53	3.22	4.49	3.85	2.24	2.38	2.73
6.35	2.04	2.92	2.53	1.56	1.61	1.67
4.75	1.49	2.17	1.87	0.94	0.97	1.18
2.00	0.57	0.69	0.76	0.32	0.32	0.42

% Passing	Combined Size[mm]	95190_1 Size[mm]	95190_2 Size[mm]	95190_3 Size[mm]	95190_4 Size[mm]	95190_5 Size[mm]
F10	25.94	20.96	23.89	31.07	28.92	27.66
F20	47.56	40.76	46.52	53.82	49.36	49.33
F30	67.72	60.31	68.71	76.27	67.65	68.35
F40	84.90	80.09	90.87	92.97	84.02	87.56
F50	105.94	98.95	111.96	111.52	100.91	106.23
F60	126.46	116.94	134.84	131.47	120.34	127.47
F63.2	134.13	123.94	142.97	138.62	127.53	134.92
F70	152.44	142.72	162.56	156.35	144.43	152.24
F80	186.96	174.28	202.51	192.14	182.73	182.14
F90	255.02	242.81	267.87	248.93	293.55	324.10
Topsize (99.95%)	485.48	413.90	451.38	418.42	471.35	556.46

Figure B.33 The combined size distribution and results of blasting pattern of 95190

APPENDIX C

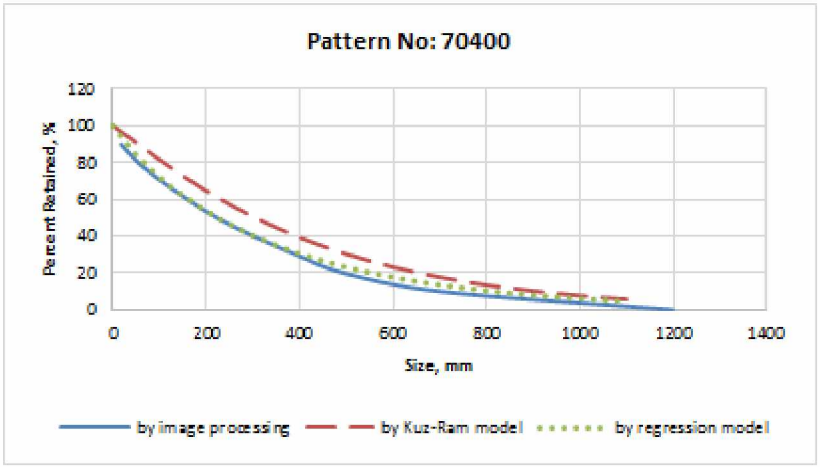

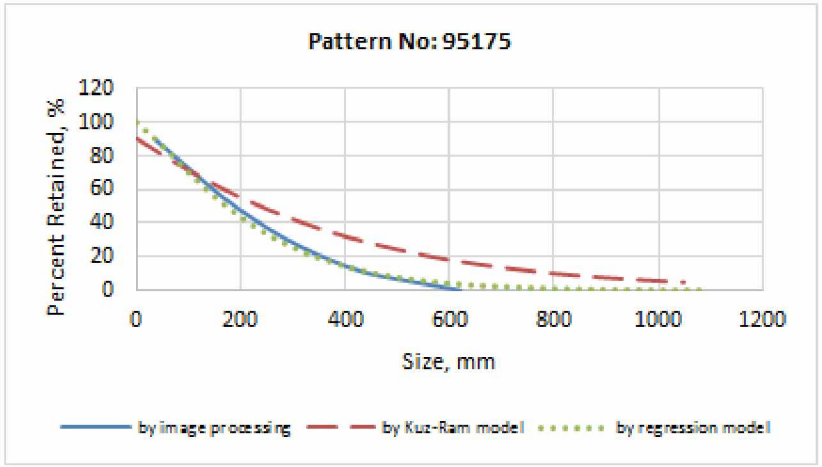

Figure C.1 Comparison of size distribution curve a) Pattern 70400, b) Pattern 95175

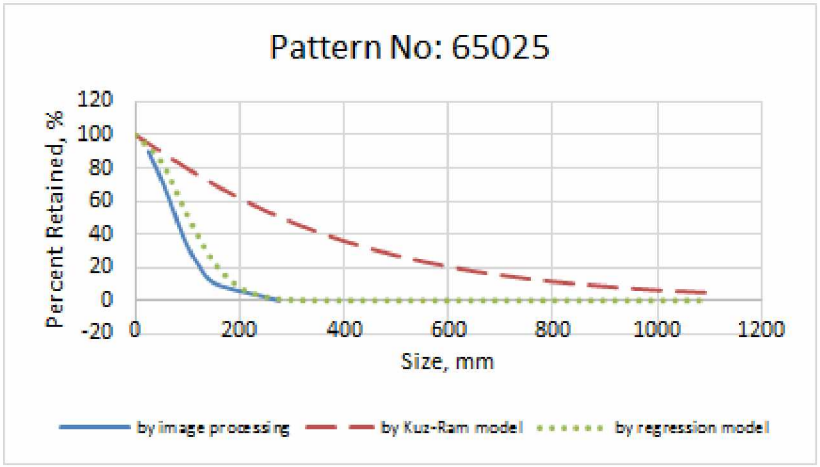

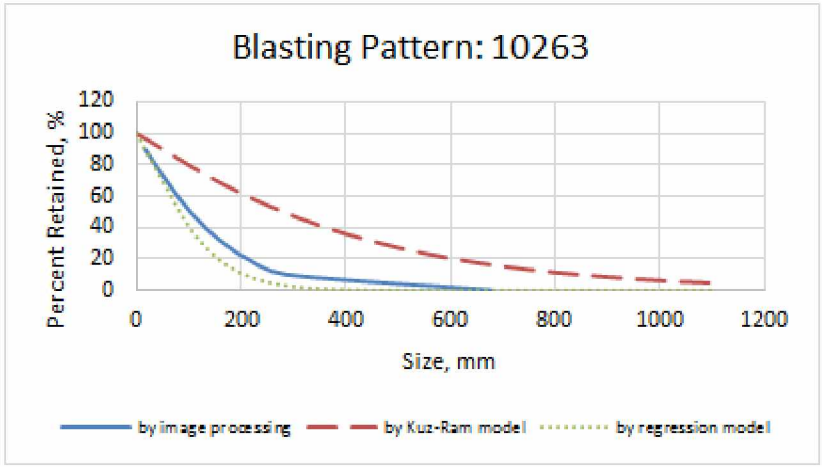

Figure C.2 Comparison of size distribution curve a) Pattern 65025, b) Pattern 10263

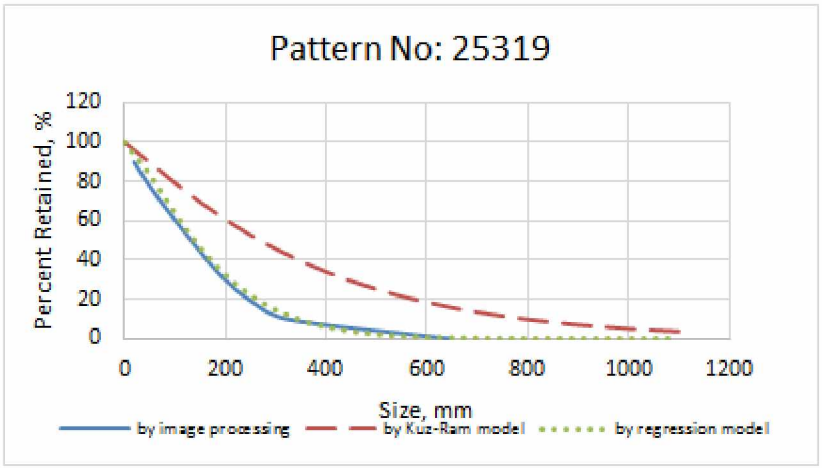

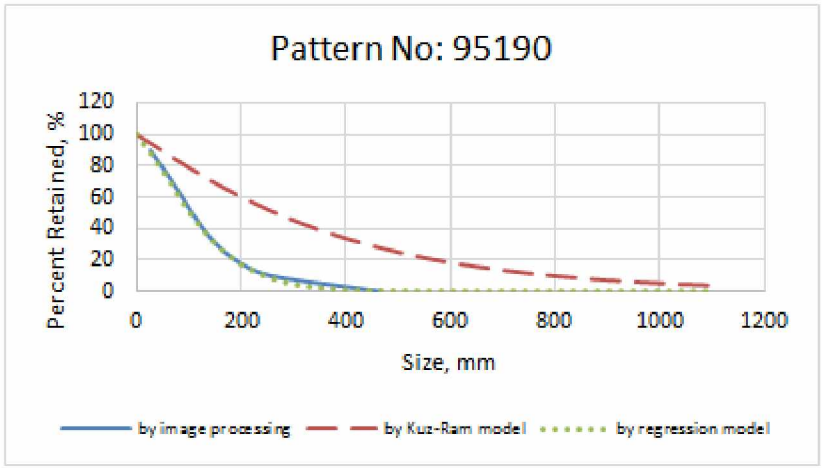

Figure C.3 Comparison of size distribution curve a) Pattern 25319, b) Pattern 95190

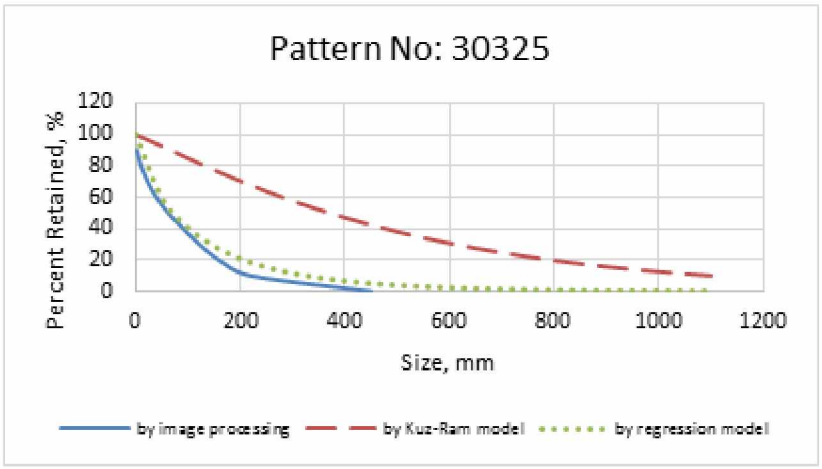

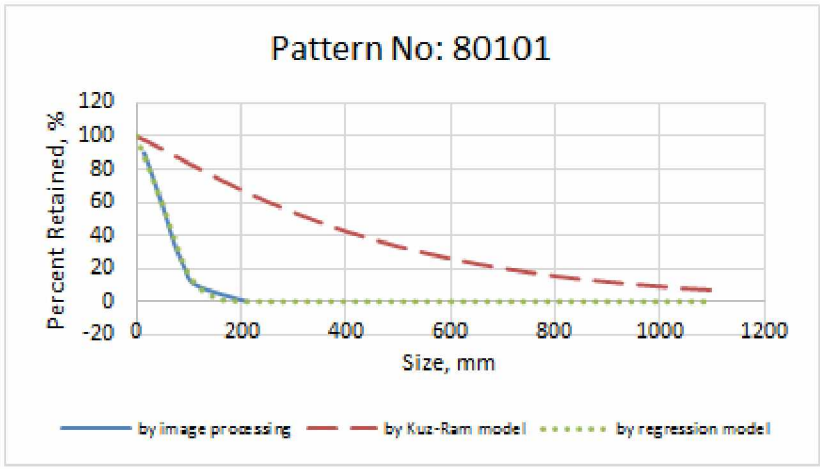

Figure C.4 Comparison of size distribution curve a) Pattern 30325, b) Pattern 80101

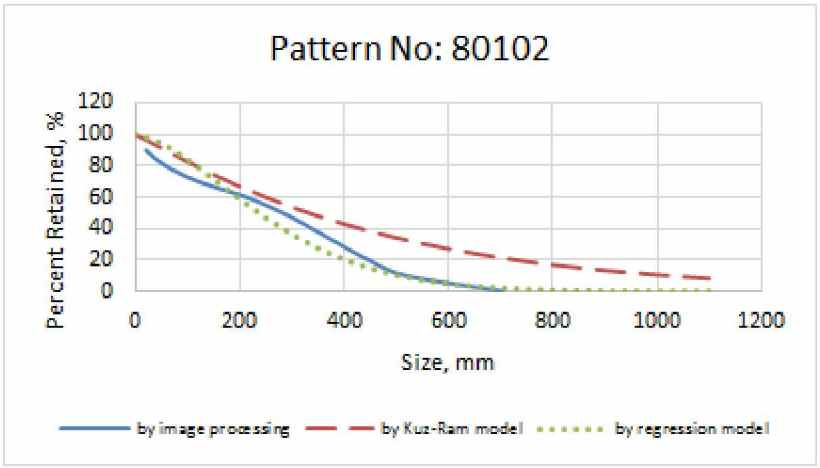

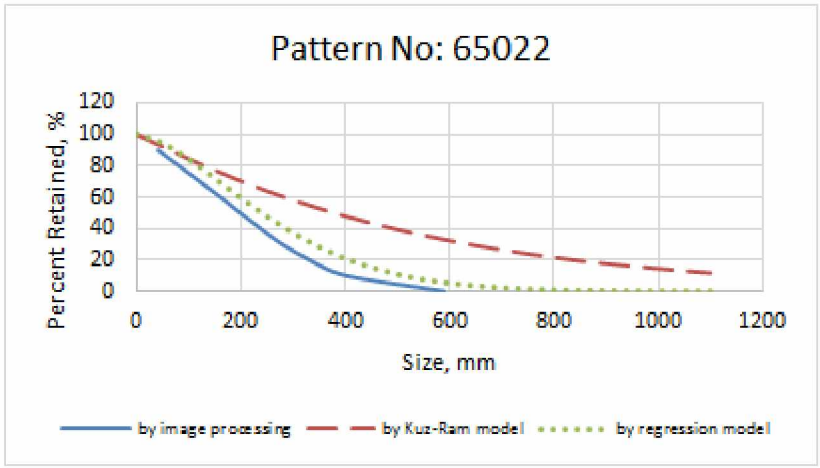

Figure C.5 Comparison of size distribution curve a) Pattern 80102, b) Pattern 65022

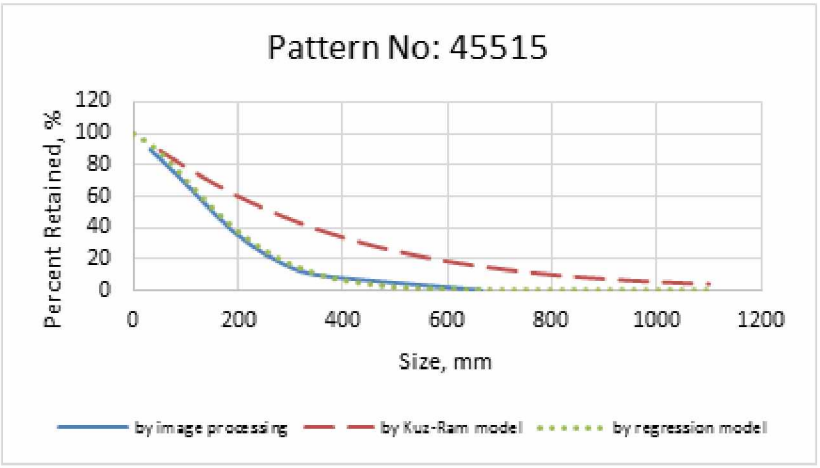

Figure C.6 Comparison of size distribution curve of Pattern 45515